

Global sensitivity analysis and uncertainty quantification of nuclear low-lying states and double-beta decay with a covariant energy density functional

X. Zhang,¹ C. C. Wang,¹ C. R. Ding,¹ and J. M. Yao^{1,*}

¹*School of Physics and Astronomy, Sun Yat-sen University, Zhuhai 519082, P.R. China*

We present a statistical analysis of nuclear low-lying states within the framework of multireference covariant density functional theory (MR-CDFT) using a relativistic point-coupling energy density functional (EDF). This study is made possible by the newly developed subspace-projected (SP)-CDFT, where the wave functions of nuclear low-lying states for target EDF parameter sets are expanded in a subspace spanned by the wave functions of low-lying states from training parameter sets. We analyze the global sensitivity of excitation energies, electric quadrupole transition strengths, and the nuclear matrix element of neutrinoless double-beta decay in ¹³⁶Xe and ¹⁵⁰Nd to EDF parameters, and explore the correlations between these quantities and nuclear matter properties. Furthermore, we quantify the statistical uncertainty of low-lying states through their posterior distributions.

I. INTRODUCTION

The nuclear density functional theory (DFT) is a microscopic self-consistent framework that offers a unified description of neutron-star matter and finite nuclei based on a universal energy density functional (EDF) [1–4]. In its simplest implementation, through self-consistent mean-field approaches, the complex nuclear many-body problem is effectively reduced to a one-body problem. The energy of a nuclear system is then approximated as a functional of the powers and gradients of nuclear densities and currents, which according to the Kohn-Sham scheme [5], can be represented in terms of auxiliary single-particle wave functions. This approach, known as single-reference (SR)-DFT, has achieved a great success in reproducing the properties of nuclear matter around saturation density and the ground states of finite nuclei across the entire nuclear chart [6–10]. Despite its success, nuclear DFT faces significant challenges due to discrepancies in predictions made by different EDFs. These discrepancies lead to considerable uncertainties, particularly for the equation of state of nuclear matter at densities far from the saturation point [11], and for neutron-rich nuclei with limited experimental data [12]. In this context, it is necessary to quantify the errors of nuclear DFT which consist of systematic and statistical components [13]. Since the currently widely used nuclear EDFs are derived from phenomenological nucleon-nucleon effective interactions—such as non-relativistic Skyrme [14, 15] and Gogny [16, 17] forces, as well as relativistic covariant EDFs [18–21]—it is difficult to quantify the systematic errors of nuclear DFT. This remains the case despite efforts to develop new generations of EDFs [22–31] inspired by effective field theories or based on ab initio calculations, as reviewed in [4, 32–34]. In contrast, the statistical error associated with a given EDF, which arises from variations in the parameters around their optimal values, can be quantified using statistical methods. Over the past decade, significant progress has been made in quantifying the statistical uncertainties of DFT predictions for nuclear ground-state bulk properties [9, 13, 35–37], and in identifying

potential correlations between nuclear matter properties [38] and neutron-star observables [39, 40].

Extending DFT to study energy spectra and transition strengths of nuclear low-lying states typically requires going beyond the mean-field approximation. In the SR-DFT, nuclear wave function is approximated as a product of auxiliary single-particle wave functions determined with the variational principle. This approach ensures the solution corresponds to a local energy minimum within the restricted Hilbert space, but it does not preserve the symmetry structure of nuclear many-body Hamiltonians. A common example is the introduction of deformation and pairing correlations in the SR-DFT for open-shell nuclei, which violate the $S(O3)$ and $U(1)$ symmetries. As a result, the quantum numbers associated with angular momentum and particle number are missing in nuclear wave functions—critical for studies of nuclear low-lying spectroscopy [41]. The restoration of broken symmetries and the inclusion of dynamical correlations from fluctuations around the equilibrium shape in the SR-DFT can be achieved through quantum-number projection and the generator coordinate method (GCM)[41, 42]. This extended framework, known as multireference DFT (MR-DFT), has been successfully applied to study nuclear low-lying states [1, 43–50], as well as the nuclear matrix elements (NMEs) of $0\nu\beta\beta$ decay [51–54].

With advances in nuclear technology and methodologies, nuclear physics is entering an era of high precision. Accurate measurements of atomic and nuclear spectroscopy in neutron-rich nuclei [55, 56], as well as the half-lives of rare nuclear processes [57–59], demand precise modeling of nuclear low-lying states and the corresponding NMEs. Therefore, quantifying the theoretical uncertainties of these physical quantities is essential for making meaningful comparisons with other models and available data. However, the uncertainties in nuclear low-lying states have been scarcely studied within EDF frameworks, primarily due to the computational intensity required for enormous repeated calculations with varying EDF parameter sets. Additionally, previous studies using the interacting shell model [60, 61] and ab initio methods [62, 63] have identified potential correlations between the NMEs of $0\nu\beta\beta$ decay and the properties of nuclear low-lying states. These correlations offer a promising approach for determining NMEs using data from nuclear low-lying states. However,

* Corresponding author: yaojm8@sysu.edu.cn

they appear to be model-dependent and vary across different nuclei, underscoring the need for further investigation with other nuclear models.

In this work, we conduct a Bayesian analysis of nuclear low-lying states and $0\nu\beta\beta$ decay using a covariant EDF, enabled by the newly developed subspace-projected covariant density functional theory (SP-CDFT) [64]. This approach integrates MR-CDFT with the eigenvector continuation (EC) method. The core idea of the EC method is to represent the eigenvector of a target Hamiltonian within a low-dimensional manifold defined by the eigenvectors of a set of sampling Hamiltonians [65]. The efficiency and accuracy of the EC method, when combined with other many-body techniques, have been demonstrated in various toy models [66–70] and in applications to nuclear structure and scattering processes [71–77], see the reviews [78, 79]. In this paper, we provide a comprehensive introduction to our SP-CDFT approach and investigate in detail the correlations between the low-lying states of near spherical and axially deformed nuclei and nuclear-matter properties at saturation density, which are commonly used to refine EDF parameters. Additionally, we perform a global sensitivity analysis of these quantities with respect to EDF parameters and quantify the statistical uncertainties in nuclear low-lying states and the NMEs of $0\nu\beta\beta$ decay using the Bayesian method.

The paper is arranged as follows. In Sec. II, we present the relevant formulas for the methods employed in this work. Sec. III presents the results of benchmark calculations, sensitivity analysis, correlation analysis, and uncertainty quantification of nuclear low-lying state properties and the NMEs of $0\nu\beta\beta$ decay. Finally, Sec. IV contains a brief summary and outlook of the present study.

II. THE METHODS

In this section, we provide a self-contained description of CDFT for finite nuclei and nuclear matter, a brief overview of MR-CDFT, and a more comprehensive introduction to SP-CDFT for nuclear low-lying states. Detailed introduction to the MR-CDFT can be found in Refs. [45, 46, 80, 81].

A. The CDFT for finite nuclei

In the SR-CDFT for finite nuclei, the nuclear wave function $|\Phi(\mathbf{q}, \mathbf{C})\rangle$ is approximated as a Slater determinant, which is a product of the wave functions ψ_k of single-particle states. These single-particle states are determined by minimizing the following covariant EDF [82, 83],

$$E[\tau, \rho, \nabla\rho; \mathbf{C}] = \int d^3r [\tau(\mathbf{r}) + \mathcal{E}^{\text{em}}(\mathbf{r}) + \mathcal{E}^{\text{int}}(\mathbf{r})]. \quad (1)$$

The first term represents the kinetic energy of nucleons,

$$\tau(\mathbf{r}) = \sum_k v_k^2 \psi_k^\dagger(\mathbf{r}) (\boldsymbol{\alpha} \cdot \mathbf{p} + \beta M - M) \psi_k(\mathbf{r}), \quad (2)$$

where $v_k^2 \in [0, 1]$ is the occupation probability of the k -th single-particle state, and its value is determined by the Bardeen–Cooper–Schrieffer (BCS) theory based on a zero-range pairing force [80]. The pairing strengths are taken as the values from Ref. [52]. The M is the nucleon bare mass. The ψ_k is a Dirac spinor, and $\boldsymbol{\alpha}, \beta$ are Dirac matrices. Using the equation of motion for the static electromagnetic field $A_\mu(\mathbf{r})$, one finds the second term in (1) for the energy of electromagnetic interaction between protons,

$$\mathcal{E}^{\text{em}}(\mathbf{r}) = \frac{e}{2} A_\mu(\mathbf{r}) j_{V,p}^\mu(\mathbf{r}) \quad (3)$$

where $j_{V,p}^\mu(\mathbf{r})$ is the proton current in coordinate space, and e is the charge of bare proton. The last term in (1) is for the energy of nucleon-nucleon effective interactions,

$$\begin{aligned} \mathcal{E}^{\text{int}}(\mathbf{r}) &= \frac{\alpha_S}{2} \rho_S^2 + \frac{\beta_S}{3} \rho_S^3 + \frac{\gamma_S}{4} \rho_S^4 + \frac{\delta_S}{2} \rho_S \Delta \rho_S \\ &\quad + \frac{\alpha_V}{2} j_\mu j^\mu + \frac{\gamma_V}{4} (j_\mu j^\mu)^2 + \frac{\delta_V}{2} j_\mu \Delta j^\mu \\ &\quad + \frac{\alpha_{TV}}{2} \mathbf{J}_{TV}^\mu \cdot (\mathbf{J}_{TV})_\mu + \frac{\delta_{TV}}{2} \mathbf{J}_{TV}^\mu \cdot \Delta (\mathbf{J}_{TV})_\mu \\ &\equiv \sum_{\ell=1}^9 c_\ell \mathcal{E}_\ell^{\text{NN}}(\mathbf{r}), \end{aligned} \quad (4)$$

which is decomposed into nine terms. Each term comes with a low-energy coupling constant (LEC) c_ℓ . All the nine LECs are collectively labeled as $\mathbf{C} = \{\alpha_S, \beta_S, \gamma_S, \delta_S, \alpha_V, \gamma_V, \delta_V, \alpha_{TV}, \delta_{TV}\}$. The subscripts (S, V) indicate the scalar and vector types of coupling vertices in Minkowski space, respectively, and T for the vector in isospin space. The symbols α_S, α_V , and α_{TV} denote the coupling constants associated with four-fermion contact interaction terms, while β_S, γ_S , and γ_V represent nonlinear self-interaction terms. Additionally, δ_S, δ_V , and δ_{TV} denote the coupling constants for gradient terms to simulate finite-range effects of nuclear force.

It is seen from (4) that the interaction energy is a functional of the local scalar density $\rho_S(\mathbf{r})$, four-component currents $j_V^\mu(\mathbf{r}), \mathbf{J}_{TV}^\mu(\mathbf{r})$ and their derivatives, where the density and currents are determined by the single-particle wave functions,

$$\rho_S(\mathbf{r}) = \sum_k v_k^2 \bar{\psi}_k(\mathbf{r}) \psi_k(\mathbf{r}), \quad (5a)$$

$$j_V^\mu(\mathbf{r}) = \sum_k v_k^2 \bar{\psi}_k(\mathbf{r}) \gamma^\mu \psi_k(\mathbf{r}), \quad (5b)$$

$$\mathbf{J}_{TV}^\mu(\mathbf{r}) = \sum_k v_k^2 \bar{\psi}_k(\mathbf{r}) \boldsymbol{\tau} \gamma^\mu \psi_k(\mathbf{r}). \quad (5c)$$

Here, $\boldsymbol{\tau}$ indicates an vector in the isospin space. The k index runs over all single-particle states under the *no-sea* approximation [20]. Minimization of the EDF in (1) with respect to $\bar{\psi}_k$ gives rise to the Dirac equation for the single nucleons

$$[\gamma_\mu (i\partial^\mu - V^\mu) - (M + \Sigma_S)] \psi_k(\mathbf{r}) = 0. \quad (6)$$

The single-particle effective Hamiltonian contains scalar $\Sigma_S(\mathbf{r})$ and vector $V^\mu(\mathbf{r})$ potentials

$$V^\mu(\mathbf{r}) = \Sigma^\mu + \boldsymbol{\tau} \cdot \Sigma_{TV}^\mu, \quad (7)$$

where

$$\Sigma_S = \alpha_S \rho_S + \beta_S \rho_S^2 + \gamma_S \rho_S^3 + \delta_S \Delta \rho_S, \quad (8a)$$

$$\Sigma^\mu = \alpha_V j_V^\mu + \gamma_V (j_V^\mu)^3 + \delta_V \Delta j_V^\mu + e A^\mu, \quad (8b)$$

$$\Sigma_{TV}^\mu = \alpha_{TV} j_{TV}^\mu + \delta_{TV} \Delta j_{TV}^\mu. \quad (8c)$$

In order to generate nuclear mean-field wave functions $|\Phi(\mathbf{q}, \mathbf{C})\rangle$ with different deformation parameters \mathbf{q} , we impose a quadrupole constraint on the mass quadrupole moment during the above minimization procedure [42, 80]. In this work, only axially-deformed parity-conserving mean-field states are considered, in which case the symbol \mathbf{q} is simply the quadrupole deformation parameter β_{20} determined by

$$\beta_{20} = \frac{4\pi}{3AR^2} \langle \Phi(\mathbf{q}, \mathbf{C}) | \hat{Q}_{20} | \Phi(\mathbf{q}, \mathbf{C}) \rangle, \quad (9)$$

where $R = 1.2A^{1/3}$ fm with A being nuclear mass number. The quadrupole moment operator is defined as $\hat{Q}_{20} = r^2 Y_{20}$, where Y_{20} is the rank-2 spherical harmonic function.

B. The CDFT for nuclear matter

The single-particle state in infinite nuclear matter is labeled with momentum $\mathbf{p} = \hbar \mathbf{k}$ and spin direction λ . The corresponding single-particle wave function is simplified into $u_\tau(\mathbf{k}, \lambda)$, which is determined by the following Dirac equation

$$(\alpha \cdot \mathbf{k} + \beta M_\tau^* + \Sigma_\tau^0) u_\tau(\mathbf{k}, \lambda) = E_\tau(\mathbf{k}) u_\tau(\mathbf{k}, \lambda), \quad (10)$$

where $\tau(n, p)$ distinguishes neutrons and protons, $M_\tau^* = M_\tau + \Sigma_{\tau S}$ is the Dirac mass. The nucleon self-energies are determined by the scalar and vector densities

$$\Sigma_{\tau S} = \alpha_S \rho_S + \beta_S \rho_S^2 + \gamma_S \rho_S^3, \quad (11a)$$

$$\Sigma_\tau^0 = \alpha_V \rho_V + \gamma_V \rho_V^3 + \alpha_{TV} \tau_3 \rho_{TV}, \quad (11b)$$

where $\rho_i = \rho_i^{(n)} + \rho_i^{(p)}$ with $i = S, V$ labeling scalar and vector densities, respectively. The isovector density is defined as the difference between the neutron and proton number densities, $\rho_{TV} = \rho_V^{(n)} - \rho_V^{(p)}$. All the densities are constant for uniformly distributed nuclear matter, for which, all the derivative terms depending on the parameters $\delta_{S,V,TV}$ vanish. For neutrons ($\tau = n$) and protons ($\tau = p$), the scalar (ρ_S) and time-like component (ρ_V) of the vector densities j_V^μ are calculated as follows,

$$\rho_S^{(\tau)} = \sum_\lambda \int_{\lambda}^{k_{\tau F}} \frac{d^3 k}{(2\pi)^3} \frac{M_\tau^*}{E_\tau(\mathbf{k})}, \quad (12a)$$

$$\rho_V^{(\tau)} = \sum_\lambda \int_{\lambda}^{k_{\tau F}} \frac{d^3 k}{(2\pi)^3} = \frac{k_{\tau F}^3}{3\pi^2}, \quad (12b)$$

where $E_{\tau F}^* = \sqrt{M_\tau^{*2} + k_{\tau F}^2}$, and λ runs over spin up and down, leading to a factor of two. At the zero temperature, the energy

density and pressure of nuclear matter are given by [84]

$$\begin{aligned} \varepsilon = \sum_\tau & \left[\frac{3}{4} (\rho_V^{(\tau)} E_{\tau F}^* - \rho_S^{(\tau)} M_\tau^*) + \rho_V^{(\tau)} M_\tau \right] \\ & + \frac{\alpha_S}{2} \rho_S^2 + \frac{\beta_S}{3} \rho_S^3 + \frac{\gamma_S}{4} \rho_S^4 + \frac{\alpha_V}{2} \rho_V^2 + \frac{\gamma_V}{4} \rho_V^4 + \frac{\alpha_{TV}}{2} \rho_{TV}^2, \end{aligned} \quad (13a)$$

$$\begin{aligned} p = \sum_\tau & \left[\frac{1}{4} (\rho_V^{(\tau)} E_{\tau F}^* - \rho_S^{(\tau)} M_\tau^*) + \Sigma_{\tau 0} \rho_V^{(\tau)} + \Sigma_{\tau S} \rho_S^{(\tau)} \right] \\ & - \frac{\alpha_S}{2} \rho_S^2 - \frac{\beta_S}{3} \rho_S^3 - \frac{\gamma_S}{4} \rho_S^4 - \frac{\alpha_V}{2} \rho_V^2 - \frac{\gamma_V}{4} \rho_V^4 - \frac{\alpha_{TV}}{2} \rho_{TV}^2. \end{aligned} \quad (13b)$$

The average nucleon binding energy E/A and incompressibility K are defined as

$$E/A \equiv \varepsilon / \rho_V - M, \quad K \equiv 9 \frac{\partial p}{\partial \rho_V}. \quad (14)$$

Besides, the symmetry energy E_{sym} and its slope parameter L are calculated by

$$E_{\text{sym}} \equiv \frac{1}{2} \left. \frac{\partial^2 (E/A)}{\partial \eta^2} \right|_{\eta=0}, \quad L \equiv 3\rho \frac{\partial E_{\text{sym}}}{\partial \rho_V}, \quad (15)$$

with the isospin asymmetry $\eta = \rho_{TV} / \rho_V$. The speed of sound is usually defined as $c_s = \sqrt{\partial p / \partial \varepsilon}$ [85], in units of the speed of light c .

C. The MR-CDFT for nuclear low-lying states

In the MR-CDFT, wave function of nuclear low-lying state is constructed as a superposition of quantum-number projected mean-field wave functions [42],

$$|\Psi_\nu^{JNZ}(\mathbf{C})\rangle = \sum_{\mathbf{q}}^{N_q} f_\nu^{JNZ}(\mathbf{q}, \mathbf{C}) |JNZ; \mathbf{q}, \mathbf{C}\rangle, \quad (16)$$

where ν distinguishes different states with the same quantum numbers JM . The basis function is constructed as

$$|JNZ; \mathbf{q}, \mathbf{C}\rangle \equiv \hat{P}_{M0}^J \hat{P}^N \hat{P}^Z |\Phi(\mathbf{q}, \mathbf{C})\rangle, \quad (17)$$

with \hat{P}_{M0}^J and $\hat{P}^{N,Z}$ are the projection operators that extract the component with the angular momentum J and its z -component $K = 0$, neutron number N , proton number Z ,

$$\hat{P}_{MK}^J = \frac{2J+1}{8\pi^2} \int d\Omega D_{MK}^{J*}(\Omega) \hat{R}(\Omega), \quad (18a)$$

$$\hat{P}^{N_\tau} = \frac{1}{2\pi} \int_0^{2\pi} d\varphi_\tau e^{i\varphi_\tau (\hat{N}_\tau - N_\tau)}, \quad (18b)$$

where $D_{MK}^{J*}(\Omega)$ is the Wigner-D function of the Euler angles Ω . The mean-field wave functions $|\Phi(\mathbf{q}, \mathbf{C})\rangle$ are generated from the above self-consistent CDFT calculation [80]. The weight function $f_\nu^{JNZ}(\mathbf{q}, \mathbf{C})$ is determined with the variational

principle which leads to the Hill-Wheeler-Griffin (HWG) equation [42, 86],

$$\sum_{\mathbf{q}'} \left[\mathcal{H}^{\mathbf{C}}(\mathbf{q}, \mathbf{q}') - E_{v,\mathbf{C}}^{JNZ} \mathcal{N}^{\mathbf{C}}(\mathbf{q}, \mathbf{q}') \right] f_v^{JNZ}(\mathbf{q}', \mathbf{C}) = 0, \quad (19)$$

where the Hamiltonian kernel and norm kernel are defined by

$$\mathcal{N}^{\mathbf{C}}(\mathbf{q}, \mathbf{q}') = \langle JNZ; \mathbf{q}, \mathbf{C} | JNZ; \mathbf{q}', \mathbf{C} \rangle, \quad (20a)$$

$$\mathcal{H}^{\mathbf{C}}(\mathbf{q}, \mathbf{q}') = \langle JNZ; \mathbf{q}, \mathbf{C} | \hat{H}(\mathbf{C}) | JNZ; \mathbf{q}', \mathbf{C} \rangle. \quad (20b)$$

The Hamiltonian kernels $\mathcal{H}^{\mathbf{C}}(\mathbf{q}, \mathbf{q}')$ are evaluated with the generalized Wick theorem [87]. In particular, the energy overlap is determined with the mixed-density prescription [48, 53].

The electric quadrupole ($E2$) transition strength for $J_{i,v_i}^\pi \rightarrow J_{f,v_f}^\pi$ from the MR-CDFT calculation of a given parameter set \mathbf{C} of EDF is determined by

$$\begin{aligned} & B^{\mathbf{C}}(E2; J_{i,v_i}^\pi \rightarrow J_{f,v_f}^\pi) \\ &= \frac{1}{2J_i + 1} \left| \sum_{\mathbf{q}, \mathbf{q}'} f_{v_f}^{J_f J_i}(\mathbf{q}', \mathbf{C}) f_{v_i}^{J_i J_f}(\mathbf{q}, \mathbf{C}) \right. \\ & \quad \left. \times \langle J_f J_i; \mathbf{q}', \mathbf{C} | \hat{Q}_2^{(e)} | J_i J_f; \mathbf{q}, \mathbf{C} \rangle \right|^2, \quad (21) \end{aligned}$$

where the reduced matrix element is determined as

$$\begin{aligned} & \langle J_f J_i; \mathbf{q}', \mathbf{C} | \hat{Q}_2^{(e)} | J_i J_f; \mathbf{q}, \mathbf{C} \rangle \\ &= (2J_f + 1)(-1)^{J_f} \sum_{\mu=-2}^2 \begin{pmatrix} J_f & 2 & J_i \\ 0 & \mu & -\mu \end{pmatrix} \\ & \quad \times \langle \Phi(\mathbf{q}', \mathbf{C}) | e r^2 Y_{2\mu} \hat{P}_{-\mu 0}^{\hat{J}_i} \hat{P}^N \hat{P}^Z | \Phi(\mathbf{q}, \mathbf{C}) \rangle. \quad (22) \end{aligned}$$

It is noted that for each parameter set of EDF, one needs to evaluate about $N_{\mathbf{q}}^2$ kernels, the calculation of which is usually very time consuming. The computational cost grows rapidly with the number of mesh points in the projection operators. Thus, it has been challenging to quantify the statistical uncertainty of the MR-CDFT study for nuclear low-lying states as it requires massive repetitive calculations based on different EDF parameter sets.

D. Emulating MR-CDFT with the SP-CDFT

In this subsection, we introduce the SP-CDFT (N_t, k_{\max}) as an emulator of the MR-CDFT for nuclear low-lying states, based on the EC method. The wave function $|\Psi_k^{JNZ}(\mathbf{C}_\odot)\rangle$ of the k -th state for a target EDF labeled with \mathbf{C}_\odot is constructed as a supposition of the wave functions $|\Psi_v^{JNZ}(\mathbf{C}_t)\rangle$ of the first k_{\max} states,

$$|\Psi_k^{JNZ}(\mathbf{C}_\odot)\rangle = \sum_{v=1}^{k_{\max}} \sum_{t=1}^{N_t} \bar{f}_{k,\mathbf{C}_\odot}^{JNZ}(v, \mathbf{C}_t) |\Psi_v^{JNZ}(\mathbf{C}_t)\rangle, \quad (23)$$

where $k \in [1, 2, \dots, k_{\max}]$. The mixing coefficient $\bar{f}_{k,\mathbf{C}_\odot}^{JNZ}(v, \mathbf{C}_t)$ is determined by the following equation,

$$\sum_{v'=1}^{k_{\max}} \sum_{t'=1}^{N_t} \left[\mathcal{H}_{tt'}^{v'v'}(\mathbf{C}_\odot) - \bar{E}_{k,\mathbf{C}_\odot}^{JNZ} \mathcal{N}_{tt'}^{v',v'} \right] \bar{f}_{k,\mathbf{C}_\odot}^{JNZ}(v', \mathbf{C}_{t'}) = 0, \quad (24)$$

Here, we define the norm and Hamiltonian kernels of the EC method for a target EDF $E[\rho, \nabla\rho; \mathbf{C}_\odot]$ as below

$$\mathcal{N}_{tt'}^{v'v'} = \langle \Psi_v^{JNZ}(\mathbf{C}_t) | \Psi_{v'}^{JNZ}(\mathbf{C}_{t'}) \rangle, \quad (25a)$$

$$\mathcal{H}_{tt'}^{v'v'}(\mathbf{C}_\odot) = \langle \Psi_v^{JNZ}(\mathbf{C}_t) | \hat{H}(\mathbf{C}_\odot) | \Psi_{v'}^{JNZ}(\mathbf{C}_{t'}) \rangle. \quad (25b)$$

The main ingredients of the SP-CDFT are the norm kernels,

$$\begin{aligned} \mathcal{N}_{tt'}^{v'v'} &= \langle \Psi_v^{JNZ}(\mathbf{C}_t) | \Psi_{v'}^{JNZ}(\mathbf{C}_{t'}) \rangle \\ &= \sum_{\mathbf{q}, \mathbf{q}'} f_v^{JNZ}(\mathbf{q}, \mathbf{C}_t) f_{v'}^{JNZ}(\mathbf{q}', \mathbf{C}_{t'}) \\ & \quad \times \langle JNZ; \mathbf{q}, \mathbf{C}_t | JNZ; \mathbf{q}', \mathbf{C}_{t'} \rangle, \quad (26) \end{aligned}$$

and Hamiltonian kernels, which can be efficiently determined as follows,

$$\begin{aligned} \mathcal{H}_{tt'}^{v'v'}(\mathbf{C}_\odot) &= \langle \Psi_v^{JNZ}(\mathbf{C}_t) | \hat{H}(\mathbf{C}_\odot) | \Psi_{v'}^{JNZ}(\mathbf{C}_{t'}) \rangle \\ &= \sum_{\mathbf{q}, \mathbf{q}'} f_v^{JNZ}(\mathbf{q}, \mathbf{C}_t) f_{v'}^{JNZ}(\mathbf{q}', \mathbf{C}_{t'}) \\ & \quad \times \langle JNZ; \mathbf{q}, \mathbf{C}_t | \hat{H}(\mathbf{C}_\odot) | JNZ; \mathbf{q}', \mathbf{C}_{t'} \rangle. \quad (27) \end{aligned}$$

For the configurations with $K = 0$, the configuration-dependent Hamiltonian kernel is simplified as

$$\begin{aligned} & \langle JNZ; \mathbf{q}, \mathbf{C}_t | \hat{H}(\mathbf{C}_\odot) | JNZ; \mathbf{q}', \mathbf{C}_{t'} \rangle \\ &= \langle \Phi(\mathbf{q}, \mathbf{C}_t) | \hat{H}(\mathbf{C}_\odot) \hat{P}_{00}^J \hat{P}^N \hat{P}^Z | \Phi(\mathbf{q}', \mathbf{C}_{t'}) \rangle \\ &= \frac{2J+1}{2} \int d_{00}^J(\cos\theta) d(\cos\theta) \int \frac{e^{-iN\varphi_n}}{2\pi} d\varphi_n \int \frac{e^{-iN\varphi_p}}{2\pi} d\varphi_p \\ & \quad \times \langle \Phi(\mathbf{q}, \mathbf{C}_t) | \hat{H}(\mathbf{C}_\odot) e^{i\theta \hat{J}_y} e^{i\varphi_n \hat{N}} e^{i\varphi_p \hat{Z}} | \Phi(\mathbf{q}', \mathbf{C}_{t'}) \rangle, \quad (28) \end{aligned}$$

where the energy overlap is evaluated with the mixed-density prescription,

$$\begin{aligned} & \frac{\langle \Phi(\mathbf{q}, \mathbf{C}_t) | \hat{H}(\mathbf{C}_\odot) e^{i\theta \hat{J}_y} e^{i\varphi_n \hat{N}} e^{i\varphi_p \hat{Z}} | \Phi(\mathbf{q}', \mathbf{C}_{t'}) \rangle}{\langle \Phi(\mathbf{q}, \mathbf{C}_t) | e^{i\theta \hat{J}_y} e^{i\varphi_n \hat{N}} e^{i\varphi_p \hat{Z}} | \Phi(\mathbf{q}', \mathbf{C}_{t'}) \rangle} \\ &= \int d^3 r \left[\tilde{\tau}(\mathbf{r}) + \tilde{\mathcal{E}}^{\text{em}}(\mathbf{r}) + \sum_{\ell=1}^9 c_\ell^\odot \tilde{\mathcal{E}}_\ell^{\text{NN}}(\mathbf{r}) \right]. \quad (29) \end{aligned}$$

All the three terms on the right hand side depend on the generate coordinates and training parameter sets, i.e., \mathbf{q}, \mathbf{q}' , and $\mathbf{C}_t, \mathbf{C}_{t'}$. Among the three terms, only the interaction energy term depends on the parameters c_ℓ^\odot of the target EDF,

$$\begin{aligned} & \sum_{\ell=1}^9 c_\ell^\odot \tilde{\mathcal{E}}_\ell^{\text{NN}}(\mathbf{q}, \mathbf{C}_t; \mathbf{q}', \mathbf{C}_{t'}) \\ &= \frac{\alpha_S^\odot}{2} \tilde{\rho}_S^2 + \frac{\beta_S^\odot}{3} \tilde{\rho}_S^3 + \frac{\gamma_S^\odot}{4} \tilde{\rho}_S^4 + \frac{\delta_S^\odot}{2} \tilde{\rho}_S \Delta \tilde{\rho}_S \\ & \quad + \frac{\alpha_V^\odot}{2} \tilde{J}_\mu \tilde{J}^\mu + \frac{\gamma_V^\odot}{4} (\tilde{J}_\mu \tilde{J}^\mu)^2 + \frac{\delta_V^\odot}{2} \tilde{J}_\mu \Delta \tilde{J}^\mu \\ & \quad + \frac{\alpha_{TV}^\odot}{2} \tilde{J}_{TV}^\mu \cdot (\tilde{J}_{TV})_\mu + \frac{\delta_{TV}^\odot}{2} \tilde{J}_{TV}^\mu \cdot \Delta (\tilde{J}_{TV})_\mu, \quad (30) \end{aligned}$$

where $\tilde{\rho}, \tilde{J}_i^\mu$ are the mixed densities and currents whose expressions have been presented in Refs. [80, 88]. They are

evaluated using the mean-field wave functions of the training sets, and thus do not depend on the parameter set \mathbf{C}_\odot of the target EDF. It enables us to speed up the calculation of the corresponding Hamiltonian kernels of target EDF. The configuration-dependent Hamiltonian kernel can be divided into parameter-free and parameter-dependent terms,

$$\begin{aligned} & \langle JNZ; \mathbf{q}, \mathbf{C}_t | \hat{H}(\mathbf{C}_\odot) | JNZ; \mathbf{q}', \mathbf{C}_{t'} \rangle \\ &= \langle JNZ; \mathbf{q}, \mathbf{C}_t | \hat{H}_0 | JNZ; \mathbf{q}', \mathbf{C}_{t'} \rangle \\ &+ \sum_{\ell=1}^9 f(c_\ell^0) \langle JNZ; \mathbf{q}, \mathbf{C}_t | \hat{H}_\ell^{NN}(\mathbf{c}_\ell^0) | JNZ; \mathbf{q}', \mathbf{C}_{t'} \rangle \end{aligned} \quad (31)$$

where the first term is given by the kinetic energy and electromagnetic energy, while the second term consists of nine NN interaction terms. During the sampling of parameter sets, we introduce a scaling factor $f(c_\ell) = c_\ell/c_\ell^0$ for each parameter in \mathbf{C} , where c_ℓ^0 is the value of the optimized parameter set of the EDF, i.e., PC-PK1 [83] in this work. The $\langle JNZ; \mathbf{q}, \mathbf{C}_t | \hat{H}_\ell^{NN}(\mathbf{c}_\ell^0) | JNZ; \mathbf{q}', \mathbf{C}_{t'} \rangle$ are the ℓ -th term in the Hamiltonian kernels with the optimized parameter set \mathbf{C}_0 sandwiched by the wave functions depending on the generate coordinates \mathbf{q}, \mathbf{q}' and training parameter sets $\mathbf{C}_t, \mathbf{C}_{t'}$. This approach allows the parameters of the EDFs in the Hamiltonian kernel of the target EDF to be factorized out. As will be shown later, this method enables the execution of millions of SP-CDFT calculations for different parameter sets of EDFs, with several orders of magnitude less computational time than MR-CDFT.

The $E2$ transition strength of the transition $J_{i,k_i}^\pi \rightarrow J_{f,k_f}^\pi$ for a target parameter set \mathbf{C}_\odot is determined by

$$\begin{aligned} & B^{\mathbf{C}_\odot}(E2; J_{i,k_i}^\pi \rightarrow J_{f,k_f}^\pi) \\ & \equiv \frac{1}{2J_i + 1} \left| \langle \Psi_{k_f}^{J_f NZ}(\mathbf{C}_\odot) | \hat{Q}_2^{(e)} | \Psi_{k_i}^{J_i NZ}(\mathbf{C}_\odot) \rangle \right|^2, \end{aligned} \quad (32)$$

where the reduced matrix elements among the states of training EDFs are given by

$$\begin{aligned} & \langle \Psi_{k_f}^{J_f NZ}(\mathbf{C}_\odot) | \hat{Q}_2^{(e)} | \Psi_{k_i}^{J_i NZ}(\mathbf{C}_\odot) \rangle \\ &= \sum_{t_i, t_f; v_i, v_f} \tilde{f}_{k_f, \mathbf{C}_\odot}^{J_f NZ}(v_f, \mathbf{C}_{t_f}) \tilde{f}_{k_i, \mathbf{C}_\odot}^{J_i NZ}(v_i, \mathbf{C}_{t_i}) \\ & \times \sum_{\mathbf{q}', \mathbf{q}} f_{v_f}^{J_f NZ}(\mathbf{q}', \mathbf{C}_{t_f}) f_{v_i}^{J_i NZ}(\mathbf{q}, \mathbf{C}_{t_i}) \\ & \times \langle J_f NZ; \mathbf{q}', \mathbf{C}_{t_f} | \hat{Q}_2^{(e)} | J_i NZ; \mathbf{q}, \mathbf{C}_{t_i} \rangle. \end{aligned} \quad (33)$$

III. RESULTS AND DISCUSSION

The Dirac equation (6) for neutrons and protons in finite nuclei is solved self-consistently by expanding the large and small components of the Dirac spinor ψ_k in a set of spherical harmonic oscillator (HO) basis with 12 major shells. The oscillator frequency is given by $\hbar\omega_0 = 41A^{-1/3}$ MeV. The Gaussian-Legendre quadrature is used for the integral over the Euler angle θ in the calculations of the norm and hamiltonian kernels in (20). We choose the number of mesh points for the

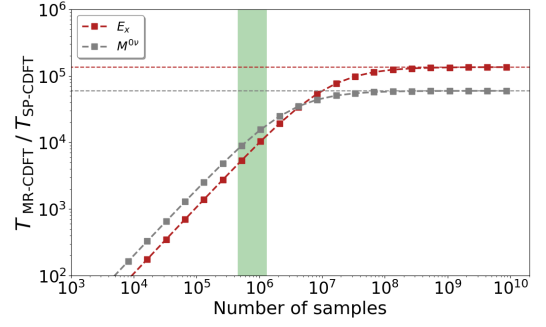


FIG. 1. (Color online) The speed-up factor of SP-CDFT calculation for nuclear low-lying states and the NME M^{0v} of $0\nu\beta\beta$ decay in ^{150}Nd . The shaded area indicates the typical sample size.

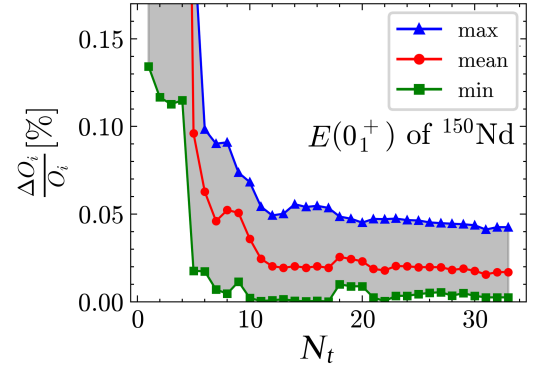


FIG. 2. (Color online) The min-max and mean values of the relative errors of the ground-state energy of ^{150}Nd from the SP-CDFT($N_t, 3$) calculations for the 64 testing sets as the function of the number N_t of training sets.

Euler angle θ in the interval $[0, \pi]$ as $N_\theta = 12$, and those for gauge angles φ_τ in the interval $[0, 2\pi]$ as $N_\varphi = 5$, which are found to be able to give convergent results. More details on the calculation of nuclear low-lying states and NME of $0\nu\beta\beta$ decay can be found in Refs. [89, 90].

A. Benchmark of SP-CDFT calculations

The time complexity of MR-CDFT calculations for $N_{\mathbf{C}_\odot}$ target parameter sets is given by

$$T_{\text{MR-CDFT}} = O(N_{\mathbf{q}}^2 N_{\mathbf{C}_\odot}) \Delta T_1, \quad (34)$$

where ΔT_1 represents the computational time for each GCM kernel. In contrast, the time complexity of the SP-CDFT(N_t, k_{max}) is composed of two parts,

$$T_{\text{SP-CDFT}} = O(N_{\mathbf{q}}^2 N_t^2) \Delta T_1 + O(N_{\text{EC}}^2 N_{\mathbf{C}_\odot}) \Delta T_2. \quad (35)$$

where the first term represents the computational time of N_t training sets, while the second term represents the time needed to evaluate the EC kernels of $N_{\mathbf{C}_\odot}$ target sets, $N_{\text{EC}} = N_t k_{\text{max}}$. It is seen that $T_{\text{SP-CDFT}} > T_{\text{MR-CDFT}}$ for $N_\odot < N_t^2$. With the

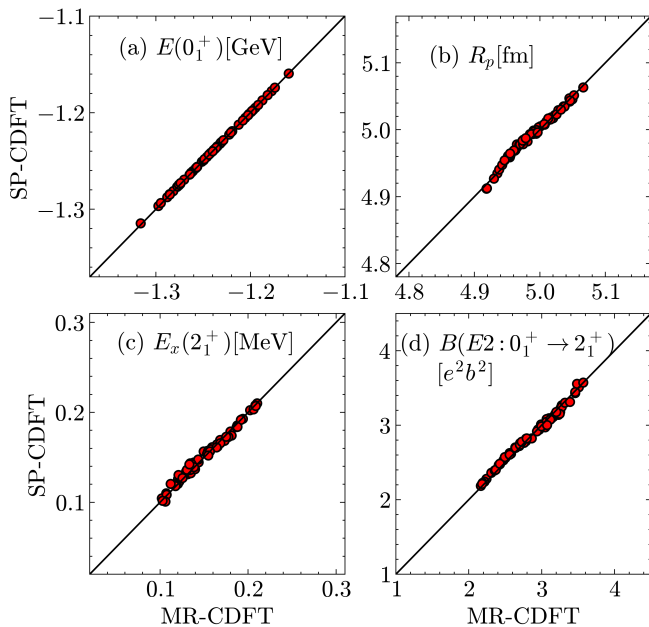


FIG. 3. (Color online) Comparison of the ground-state properties and low-lying states properties from the SP-CDFT(14,3) and MR-CDFT calculations for ^{150}Nd based on 64 testing EDFs.

increase of N_{C_\odot} , both $T_{\text{MR-CDFT}}$ and $T_{\text{SP-CDFT}}$ increase linearly, but with the slopes of $N_q^2 \Delta T_1$ and $N_{\text{EC}}^2 \Delta T_2$, respectively. By breaking the interaction energy (4) into nine terms, one can compute the Hamiltonian kernels of EC efficiently using the GCM kernels of the training EDFs, see Eq.(31). Quantitatively, we find $\Delta T_1 / \Delta T_2 \approx 10^5$ for ^{150}Nd . In other words, one would expect $T_{\text{SP-CDFT}} \ll T_{\text{MR-CDFT}}$ when the number of target sets N_{C_\odot} is sufficient large.

Figure 1 displays the speed-up factor, defined as the ratio of $T_{\text{MR-CDFT}}$ to $T_{\text{SP-CDFT}}$ for nuclear low-lying states and the NME $M^{0\nu}$ of $0\nu\beta\beta$ decay, as a function of N_{C_\odot} . The $M^{0\nu}$ is computed using the transition operators based on the standard mechanism, see Refs. [52, 90] for details. Since the $T_{\text{MR-CDFT}}$ increases linearly with the number of samples, and the $T_{\text{SP-CDFT}}$ is barely changing with it, the speed-up factor $T_{\text{MR-CDFT}}/T_{\text{SP-CDFT}}$ increases almost linearly up to 10^4 when the number of sampling EDFs reaches to 10^6 . It is also seen from Fig. 1 that the speed-up factor reaches asymptotically a limit as the number of samples increases up to 10^8 , i.e., $T_{\text{MR-CDFT}}/T_{\text{SP-CDFT}} \rightarrow (N_q/N_{\text{EC}})^2 (\Delta T_1/\Delta T_2)$. A similar behavior has been found in Ref. [72]. In short, the SP-CDFT allows us, within half an hour using a PC, to predict nuclear low-lying states for millions of EDFs which would otherwise take years with the MR-CDFT.

The accuracy of SP-CDFT(N_t, k_{max}) depends on the selected values of N_t and k_{max} . As demonstrated in Ref.[64], choosing $k_{\text{max}} \geq 3$ effectively reproduces the excitation energy of the 2_1^+ state. Figure 2 shows the relative error in the ground-state energy of ^{150}Nd from SP-CDFT($N_t, k_{\text{max}} = 3$) calculations across 64 test sets. Both the training sets and testing sets are sampled using the Latin hypercube sampling method[91], which is commonly used to generate a represen-

TABLE I. The errors $\sigma(O)$ and relative errors $\mathcal{R}(O) = \sigma(O)/O^{\text{MR-CDFT}}$ of the SP-CDFT calculations, compared to the results of MR-CDFT, based on 64 parameter sets of EDFs for the ground-state energy $E(0_1^+)$ and proton radius R_p , the excitation energy $E_x(2_1^+)$, and $B(E2: 0_1^+ \rightarrow 2_1^+)$ of ^{150}Nd and ^{150}Sm .

Nuclei	$E(0_1^+)$ (MeV)		R_p (fm)		$E_x(2_1^+)$ (MeV)		$B(E2)$ ($e^2 b^2$)	
	σ	$\mathcal{R}[\%]$	σ	$\mathcal{R}[\%]$	σ	\mathcal{R}	σ	$\mathcal{R}[\%]$
^{150}Nd	0.272	0.02	0.003	0.2	0.006	4	0.063	2
^{150}Sm	0.180	0.01	0.005	0.1	0.040	13	0.071	4

tative sample of parameter values from a multidimensional distribution [36, 92–94]. Here, a uniform distribution is chosen as the probability distribution. The parameter ranges for Latin hypercube sampling are selected based on the uncorrelated tolerance of parameters with $\chi^2 \leq \chi_{\text{min}}^2 + 1$. As shown in Fig. 2, as N_t increases to 14, the mean relative error decreases to 0.04% and stabilizes. Consequently, we select $N_t = 14$ for the subsequent calculations.

Figure 3 compares the ground-state energies, root-mean-square (rms) proton radii, excitation energies $E_x(2_1^+)$, and $B(E2: 0_1^+ \rightarrow 2_1^+)$ values obtained from SP-CDFT (14, 3) and MR-CDFT calculations for ^{150}Nd using 64 test sets. The data points align along the diagonal line, indicating strong agreement between the two methods. To quantify the accuracy of the emulator, we define the error of the SP-CDFT calculation compared to MR-CDFT as follows

$$\sigma[O] = \sqrt{\frac{1}{N_t} \sum_{i=1}^{N_t} \left(O_i^{\text{SP-CDFT}} - O_i^{\text{MR-CDFT}} \right)^2}. \quad (36)$$

Table I presents the errors and relative errors for these four quantities in ^{150}Nd and ^{150}Sm . The ground-state energy $E(0_1^+)$ and the proton radius R_p are reproduced with relative errors of 0.02% and 0.2%, respectively. However, the emulator error for the excitation energy $E_x(2_1^+)$, which is several orders of magnitude smaller than the binding energy, is relatively larger, with a relative error of 13%. The E2 transition strengths are reproduced with better accuracy. We also checked the relative errors of the SP-CDFT calculations for ^{136}Xe and ^{136}Ba , finding them to be generally less than 6%.

B. Global sensitivity analysis

Figure 4 illustrates the variation of physical quantities such as $E(0_1^+)$, $E_x(2_1^+)$, and $B(E2: 0_1^+ \rightarrow 2_1^+)$ for low-lying states, as well as the NME $M^{0\nu}$ for $0\nu\beta\beta$ decay in ^{150}Nd , with respect to each parameter c_ℓ of the EDF. The results show that $E(0_1^+)$ and $E_x(2_1^+)$ increase (or decrease) smoothly with α_V (or α_S). In contrast, Figure 5 reveals that while the ground-state energy $E(0_1^+)$ of ^{136}Xe follows a similar trend, increasing with α_V and decreasing with α_S , its excitation energy $E_x(2_1^+)$ displays an opposite trend compared to the prolate deformed nucleus ^{150}Nd . The trends for $B(E2: 0_1^+ \rightarrow 2_1^+)$ in these two nuclei

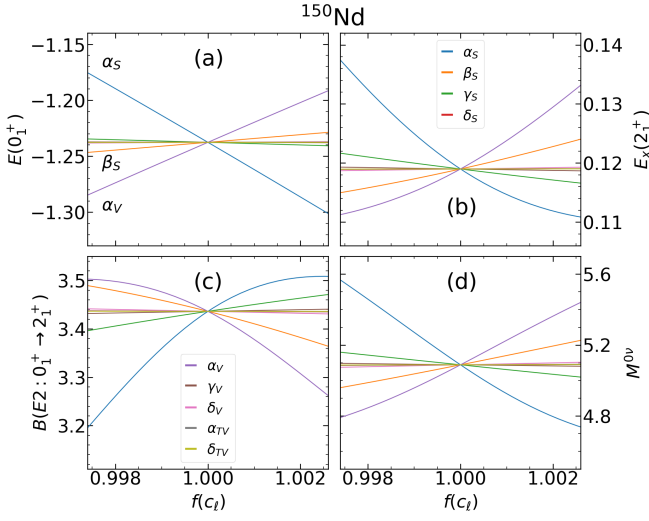


FIG. 4. (Color online) (a) The ground-state energy $E(0_1^+)$ (GeV), (b) excitation energy $E_x(2_1^+)$ (MeV) of 2_1^+ state, the E2 transition strength $B(E2: 0_1^+ \rightarrow 2_1^+)$ (e^2b^2), and M^{0v} in ^{150}Nd as a function of $f(c_l)$ from the SP-CDFT(14, 3) calculation, where $f(c_l) = 1$ corresponds to the value of the PC-PK1 [83].

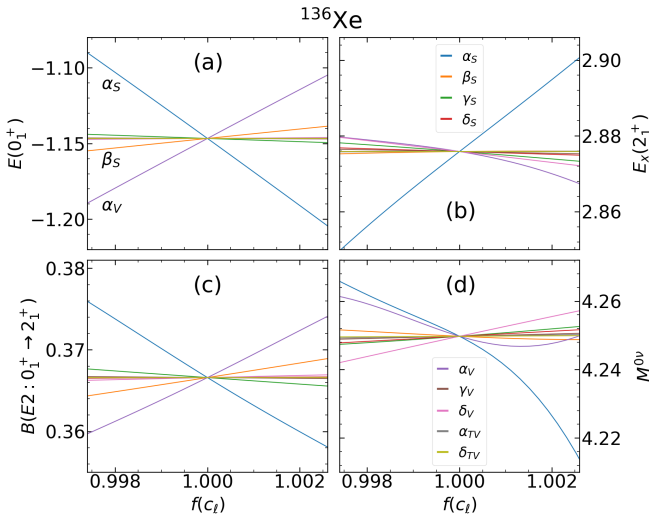


FIG. 5. (Color online) Same with Fig. 4, but for ^{136}Xe .

also differ. Additionally, it is noteworthy that the NME M^{0v} in ^{150}Nd decreases with increasing α_s and increases with α_v . In contrast, the NME M^{0v} in ^{136}Xe decreases with both α_s and α_v around their values in PC-PK1, with changes in these quantities being much less sensitive to other parameters.

Subsequently, we conduct a global sensitivity analysis (GSA) of the nine parameters in the MR-CDFT calculations for nuclear low-lying states. A similar approach has been employed using an emulator of coupled-cluster theory based on nuclear chiral interactions [71]. GSA provides a method to determine how the uncertainty in a calculated quantity Y is attributed to the uncertainties in each input parameter c_l , where $\mathbf{C} = \{c_{i=1,\dots,9}\}$. The total variance of Y can be decomposed as

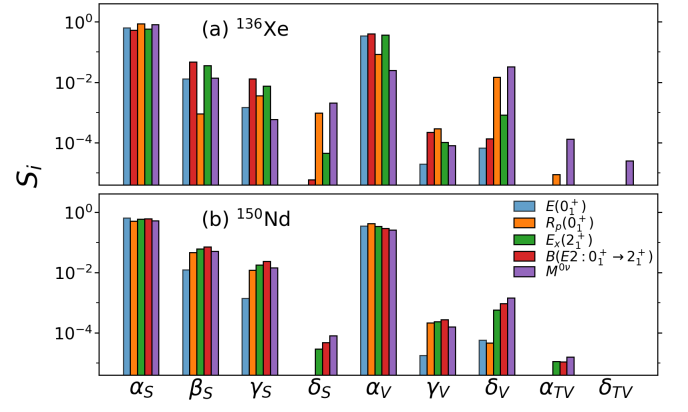


FIG. 6. (Color online) The first-order sensitivity index S_i of the ground-state energy $E_x(0_1^+)$ and proton radius $R_p(0_1^+)$, excitation energy of 2_1^+ state, the $B(E2: 0_1^+ \rightarrow 2_1^+)$, and M^{0v} in (a) ^{136}Xe and (b) ^{150}Nd . See text for details.

follows [95],

$$\text{Var}(Y) = \sum_{i=1}^{d=9} V_i + \sum_{i<j}^{d=9} V_{ij} + \dots + V_{12\dots 9}, \quad (37)$$

where

$$V_i = \text{Var}(E_{C_i}(Y | c_i)), \quad (38)$$

$$V_{ij} = \text{Var}(E_{C_{ij}}(Y | c_i, c_j)) - V_i - V_j, \quad (39)$$

and so on. The V_i denotes the variance of $E_{C_i}(Y | c_i)$, which is the conditional expectation of Y for the i -th parameter,

$$E_{C_i}(Y | c_i) = \frac{1}{N_Y} \sum_{n=1}^{N_Y} Y^{(n)}(\mathbf{C}_i). \quad (40)$$

Here, $\{Y^{(n)}(\mathbf{C}_i)\}$ are a set of calculated values for Y using all the parameter sets for a fixed value of c_i . The \mathbf{C}_i notation indicates the set of all the nine parameters excluding c_i . The V_i gives the leading-order contribution to the variance of Y from the i -th parameter c_i . One usually introduces a normalized quantity

$$S_i = \frac{V_i}{\text{Var}(Y)}, \quad S_{ij\dots} = \frac{V_{ij\dots}}{\text{Var}(Y)}. \quad (41)$$

The S_i is called the "first-order sensitivity index", or "main effect index". The rest terms on the right hand side of Eq.(37) usually give minor contributions. The total effective index S_i^T of the i -th parameter is defined as,

$$S_i^T = S_i + \sum_{j=1}^d S_{i,j} + \dots \quad (42)$$

which fulfils the normalization condition [95],

$$\sum_{i=1}^d S_i^T = 1. \quad (43)$$

TABLE II. The values of the PC-PK1 parameter set of the relativistic EDF and the ranges of the parameters in the training and target sets of the EDF.

c_ℓ	PC-PK1 [83]	dimension	training sets[%]	target sets[%]
α_S	-3.96291×10^{-4}	MeV^{-2}	0.5	0.1
β_S	$+8.6653 \times 10^{-11}$	MeV^{-5}	2	1
γ_S	-3.80724×10^{-17}	MeV^{-8}	4	2
δ_S	-1.09108×10^{-10}	MeV^{-4}	20	4
α_V	$+2.69040 \times 10^{-4}$	MeV^{-2}	0.8	0.2
γ_V	-3.64219×10^{-18}	MeV^{-8}	30	5
δ_V	-4.32619×10^{-10}	MeV^{-4}	20	5
α_{TV}	$+2.95018 \times 10^{-5}$	MeV^{-2}	10	6
δ_{TV}	-4.11112×10^{-10}	MeV^{-4}	150	40

Figure 6 presents the values of S_i from the global sensitivity analysis (GSA) for various quantities, including the ground-state energy $E_x(0_1^+)$, proton root-mean-square radius R_p , excitation energies of the 2_1^+ and 4_1^+ states, $E2$ transition strength, and $M^{0\nu}$ for ^{150}Nd and ^{150}Sm . To ensure that the model response remains within a physically reasonable range, we sample a parameter domain corresponding to a 0.5% variation around the PC-PK1 value. The results indicate that approximately 90% of the variance in all these quantities is attributed to the parameters α_s and α_v , with secondary contributions from β_s and γ_s , which account for most of the remaining variance. Similar patterns are observed in ^{136}Xe and ^{136}Ba . This suggests that these parameters can be effectively determined by nuclear low-lying states. Additionally, we find that $S_i^T \approx S_i$ for all parameters, as expected.

C. Bayesian statistical analysis

We sampled a total of $(9+1) \times 2^{17} \approx 1.3 \times 10^6$ EDF parameter sets by varying all nine parameters around the PC-PK1 values [83] using quasi Monte-Carlo (MC) sampling with a uniform distribution within the ranges shown in Table II. Using these parameter sets, we calculated the properties of infinite nuclear matter as a function of nucleon number density ρ_V , as illustrated in Fig. 7. For comparison, results from many-body perturbation theory based on a chiral Hamiltonian [85] are also presented, revealing significant discrepancies between the two approaches. The physical quantities at saturation density ρ_0 , denoted as $\Theta_{\text{sat}} = \{\rho_0, E/A, E_{\text{sym}}, L, K\}$, calculated from the sampled EDF parameter sets, are displayed in Fig. 8. We observe some mismatches between the mean values of ρ_0 and E_{sym} and their empirical values. To incorporate refinements from nuclear matter into the EDFs, we introduce the implausibility function[96]

$$I_{(i)}(\mathbf{C}) = \sqrt{\frac{[O_{(i)}^{\text{calc.}}(\mathbf{C}) - O_{(i)}^{\text{empi.}}]^2}{\sigma^2(O_{(i)}^{\text{empi.}})}}. \quad (44)$$

Here, $\sigma(O_{(i)}^{\text{empi.}})$ denotes the standard deviation of the empirical value for the i -th physical quantity of infinite nuclear matter. The implausibility function $I(i)(x)$ measures the

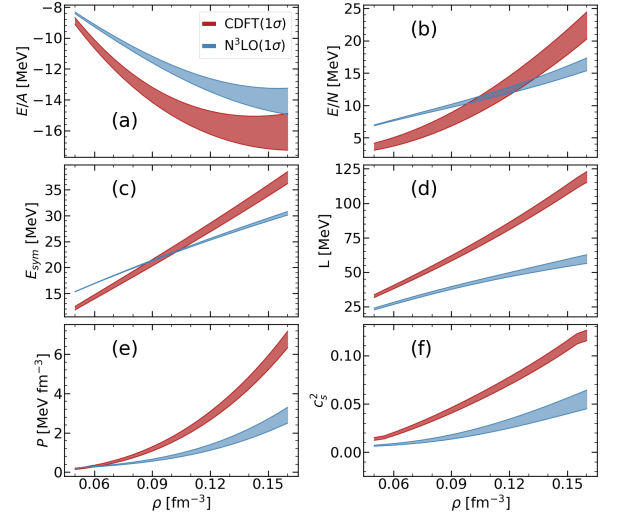


FIG. 7. (Color online) (a) The energy per particle E/A for symmetric nuclear matter, (b) the energy per neutron E/N for pure neutron matter, (c) symmetry energy E_{sym} , (d) the symmetry energy slope L , (e) pressure P , and (f) the square of the speed of sound c_s^2 are calculated using about one million samples from the covariant EDF. The results are compared with those, labeled as $N^3\text{LO}$, from ab initio many-body perturbation theory calculations based on a chiral Hamiltonian by Drischler et al. [85].

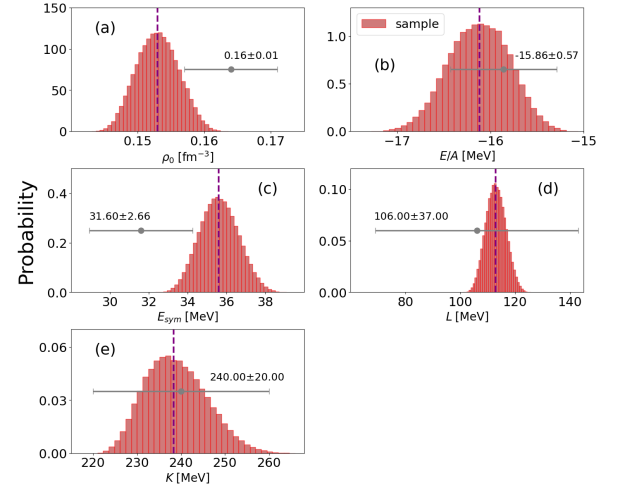


FIG. 8. (Color online) Histogram plots of nuclear-matter properties around saturation density calculated using $(9+1) \times 2^{17} = 1310720$ quasi MC samples of the nine coupling constants in the relativistic EDFs around the PC-PK1 parametrization [83]. The empirical values (gray error bar) are given for comparison. The numbers are empirical values.

probability that the theoretically calculated value $O^{\text{calc.}}(i)(x)$ matches the empirical value $O^{\text{empi.}}(i)$. We screen the parameter sets \mathbf{C} based on the criterion $\max[I_{(i)}(x)] < \sqrt{3}$, which corresponds to a probability of about 92%. Here, $\max[I_{(i)}(x)]$ represents the largest value of the implausibility functions across the physical quantities Θ_{sat} of infinite nuclear matter. After applying the $\sqrt{3}\sigma$ screening rule using the properties of nu-

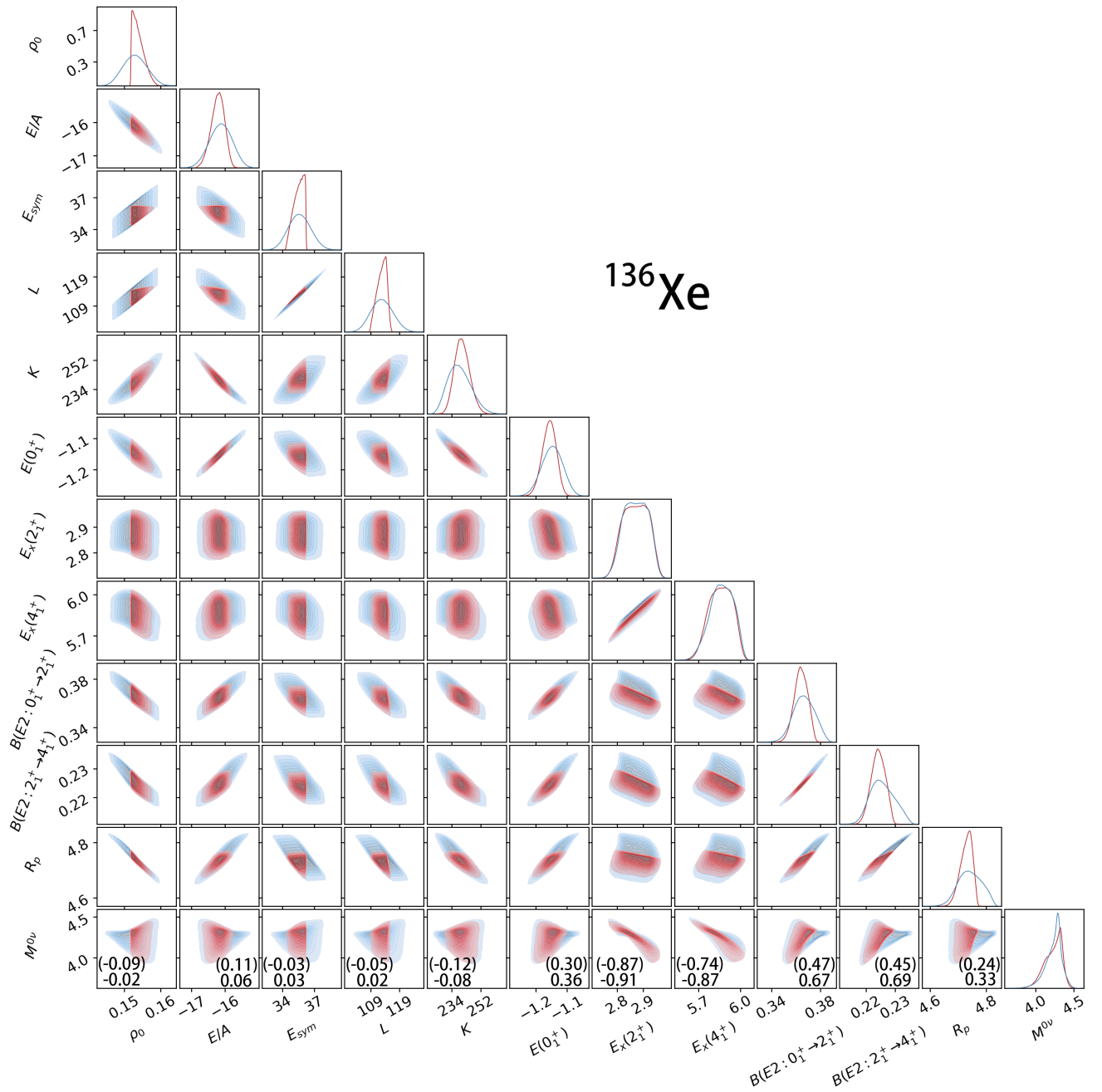


FIG. 9. (Color online) The correlation relation among different quantities. The diagonal diagrams are the histograms for the probability distributions of these quantities for ^{136}Xe . The red distributions are refined by the empirical values of the physical quantities $\Theta_{\text{sat}} = \{\rho_0, E/A, E_{\text{sym}}, L, K\}$ of infinite nuclear matter at saturation density using $\sqrt{3}\sigma$ rule. In the bottom row, the Pearson coefficients are derived from the red distributions, while those in parentheses are based on the blue distributions. See main text for details.

clear matter, we obtain a final set of 457,380 non-implausible samples. Using the above samples, we calculated the physical quantities of nuclear low-lying states with SP-CDFT(14, k_{max}) for ^{150}Nd , ^{150}Sm , ^{136}Xe , and ^{136}Ba . The results for ^{136}Xe and ^{150}Nd , with and without refinement from nuclear matter properties, are shown in blue and red in Figs. 9 and 10, respectively. Since the results for ^{150}Sm closely resemble those for ^{150}Nd , and those for ^{136}Ba are similar to ^{136}Xe , we

do not display them here. Our findings from these figures are as follows:

- Correlations among nuclear-matter properties and the bulk properties of finite nuclei reveal that the slope parameter L of the symmetry energy and the average nucleon energy E/A of nuclear matter are strongly positively correlated with the symmetry energy E_{sym} and the nuclear ground-state energy $E(0_1^+)$, respectively. Addi-

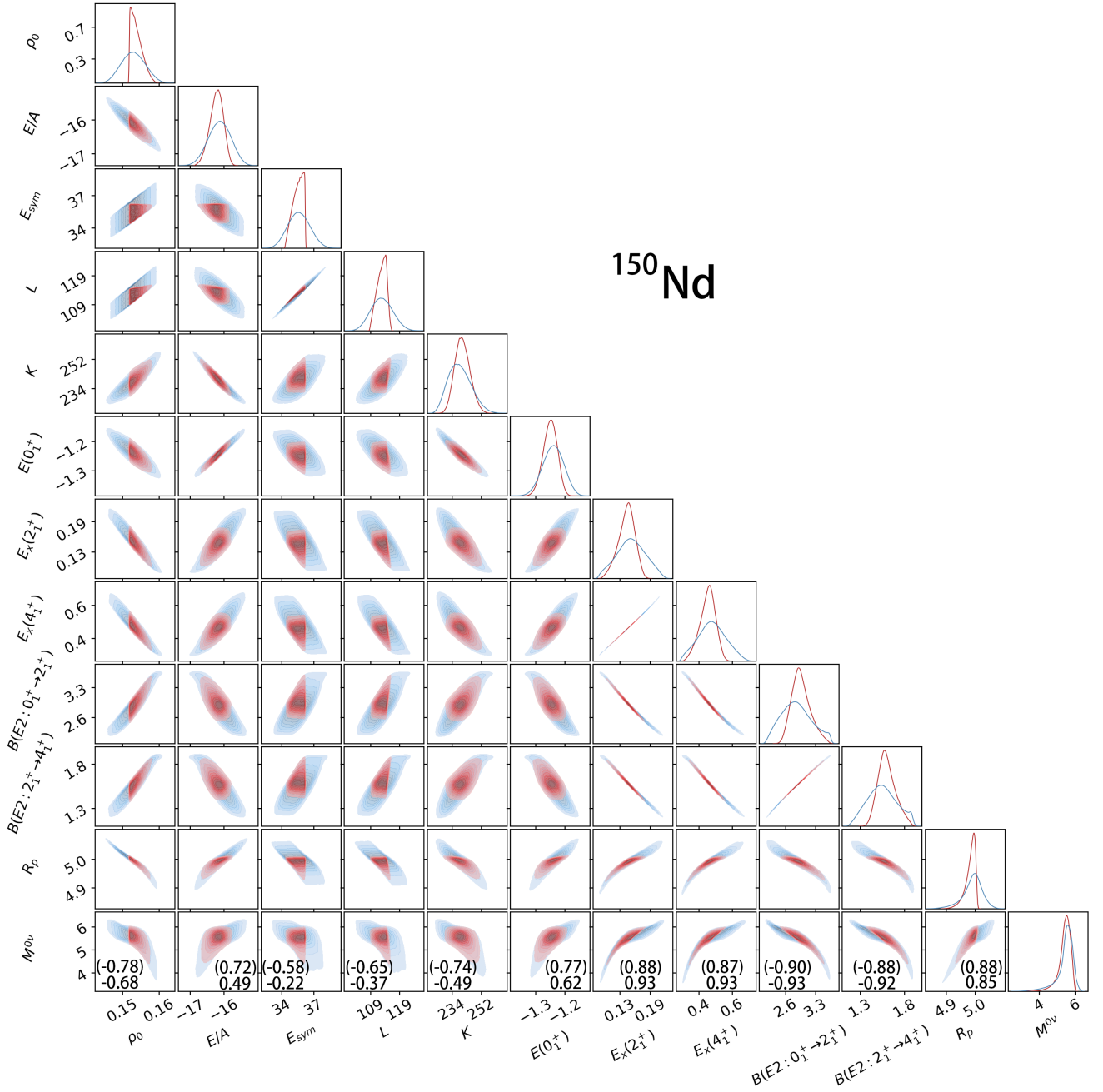


FIG. 10. (Color online) Same as Fig. 9, for ^{150}Nd .

tionally, the saturation density ρ_0 and the average nucleon energy E/A of symmetric nuclear matter are anti-correlated with the proton radius R_p of finite nuclei and the incompressibility K of the nuclear matter, respectively. These correlation patterns are found to be similar in ^{150}Nd and ^{136}Xe .

- Correlations among nuclear low-lying states reveal that the excitation energies of the 2_1^+ and 4_1^+ states are anti-correlated with the $E2$ transition strengths. This correlation is strong in the deformed nuclei ^{150}Nd and ^{150}Sm , but very weak in the spherical nuclei ^{136}Xe and

^{136}Ba . Interestingly, the proton radius R_p of the ground state is positively correlated with the $B(E2: 0_1^+ \rightarrow 2_1^+)$ in ^{136}Xe , while it is anti-correlated in ^{150}Nd . To understand the anti-correlation behavior in ^{150}Nd , we plot the unnormalized mean-squared radii \bar{R}_p^2 against the unnormalized reduced $E2$ transition matrix element $|\bar{Q}_p|$ from single-configuration calculations using different EDF parameter sets in Fig.11. These are shown to be strongly positively correlated, as expected. Since the normalization factor $\sqrt{N_0}$ of the $J = 0$ state is also linearly correlated with the normalization factor $\sqrt{N_2}$ of

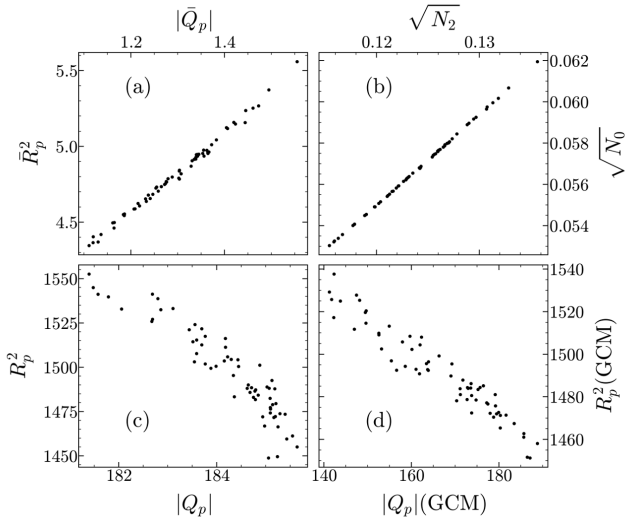


FIG. 11. (a), (b), (c) The correlations among mean-squared radius $R_p^2 = N_0^{-1} \langle J = 0NZ; \beta_2, \mathbf{C} | \hat{R}_p^2 | J = 0NZ; \beta_2, \mathbf{C} \rangle$, reduced $E2$ transition matrix element $Q_p = (N_0 N_2)^{-1/2} \langle J = 2NZ; \beta_2, \mathbf{C} | \hat{Q}_2 | J = 0NZ; \beta_2, \mathbf{C} \rangle$ and normalization factors $\sqrt{N_J}$ from the calculations for ^{150}Nd based on a single configuration with $\beta_2 = 0.3$, where $N_J = \langle JNZ; \beta_2, \mathbf{C} | JNZ; \beta_2, \mathbf{C} \rangle$. (d) The results from the configuration-mixing GCM calculations. The quantities hatted with bars are unnormalized. See main text for details.

the $J = 2$ state with a nonzero intercept, it results in an anti-correlation between the normalized mean-squared radii R_p^2 and the normalized reduced $E2$ transition matrix element $|Q_p|$, as illustrated in Fig.11(c). This anti-correlation persists in the configuration-mixing GCM calculation, as shown in Fig. 11(d). In short, the $B(E2 : 0_1^+ \rightarrow 2_1^+)$ could be either positive or negative correlated with the proton radius R_p of the ground state.

Subsequently, we use the Bayesian method to derive the posterior distribution $p(O|\mathcal{D})$ for the quantity O given the data \mathcal{D} (which includes nuclear-matter properties, among other things). This posterior distribution can be expressed as an integral that incorporates statistical information from various parameter sets:

$$p(O|\mathcal{D}) = \int p(O|\mathbf{C})p(\mathbf{C}|\mathcal{D})d\mathbf{C}. \quad (45)$$

Here, $p(\mathbf{C}|\mathcal{D})$ represents the posterior distribution of the model parameters \mathbf{C} and can be determined using Bayes' theorem:

$$p(\mathbf{C}|\mathcal{D}) = \frac{p(\mathcal{D}|\mathbf{C})\pi(\mathbf{C})}{p(\mathcal{D})}. \quad (46)$$

In this equation, $p(\mathcal{D})$ serves as a normalization constant. The prior distribution $\pi(\mathbf{C})$ of the parameters reflects the empirical evaluation of each parameter set \mathbf{C} . Here, we use an uncorrelated multivariate normal distribution,

$$\pi(\mathbf{C}) \propto \exp(-\chi_0^2/2), \quad \chi_0^2 = \sum_{\ell=1}^9 \frac{(c_\ell - c_\ell^0)^2}{\sigma_\ell^2}, \quad (47)$$

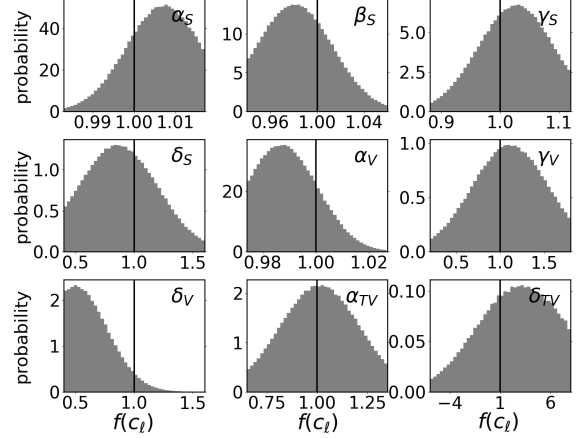


FIG. 12. The posterior distributions $p(\mathbf{C}|\mathcal{D})$, defined in (46), for the nine parameters (normalized to PC-PK1) in the relativistic EDF from the Bayesian analysis, where the data \mathcal{D} contain the empirical values of nuclear matter at saturation density Θ_{sat} , the Θ_{low} of nuclear matter below saturation density from the chiral nuclear force, and the data for the $B(E2 : 0_1^+ \rightarrow 2_1^+)$ of ^{136}Xe .

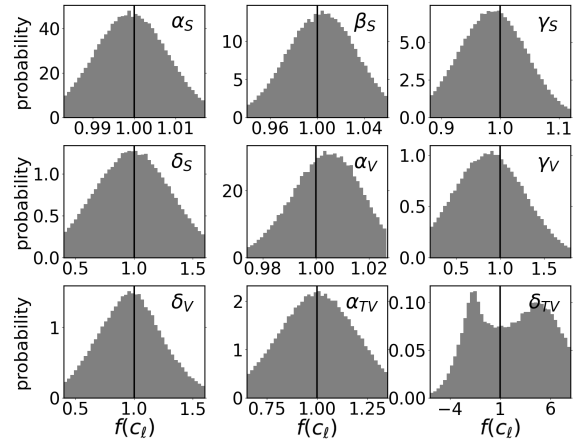


FIG. 13. Same as Fig. 12, but replacing the data for the $B(E2 : 0_1^+ \rightarrow 2_1^+)$ of ^{136}Xe with that of ^{150}Nd .

where c_ℓ^0 is the value of the ℓ -th parameter in the PC-PK1 set, and σ_ℓ is the standard deviation of the parameter c_ℓ in the samples from the quasi MC sampling method as mentioned before.

The likelihood function $p(\mathcal{D}|\mathbf{C})$ also takes the form of multivariate normal distribution

$$p(\mathcal{D}|\mathbf{C}) \propto \exp(-\chi^2/2), \quad \chi^2 = \sum_{i=1}^{N_{\text{obs}}} \frac{(D_i^{\text{em}}(\mathbf{C}) - D_i^{\text{exp}})^2}{\sigma_i^2}, \quad (48)$$

where σ_i denotes the standard deviation of the data D_i^{exp} . The

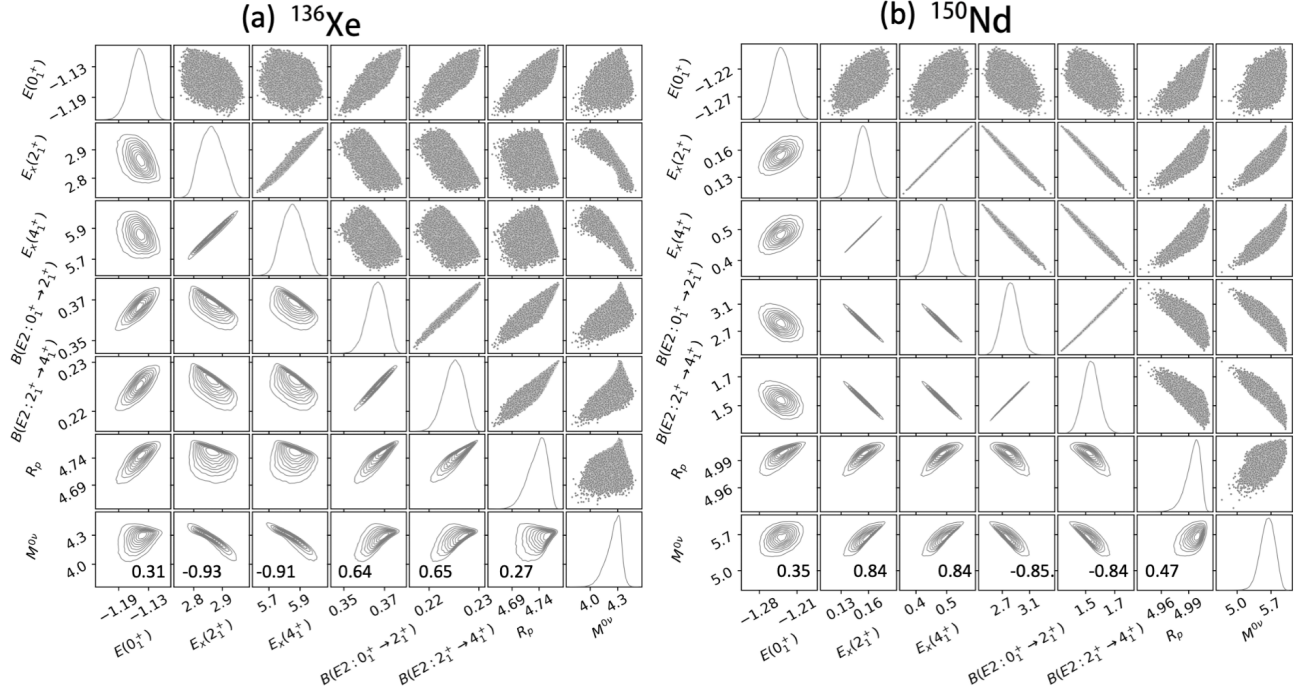


FIG. 14. The correlations among the quantities of nuclear matter at saturation density, nuclear low-lying states and the NME of $0\nu\beta\beta$ decay from their posterior distributions $p(\mathbf{C}|\mathcal{D})$ shown in Fig. 13. (a) is for the results of ^{136}Xe , while (b) is for those of ^{150}Nd . The numbers in the bottom row are the Pearson coefficients.

TABLE III. The median, 4th percentile, and 96th percentile (corresponding to 92% C.L.) of the excitation energies (in MeV) of 2_1^+ and 4_1^+ states and $E2$ transition strengths (in e^2b^2) derived from the posteriors of the SP-CDFT calculations for ^{150}Nd , ^{150}Sm , ^{136}Xe , and ^{136}Ba , in comparison with available data [97].

	$E_x(2_1^+)$	$E_x(4_1^+)$	$B(E2 : 2_1^+ \rightarrow 4_1^+)$	$B(E2 : 0_1^+ \rightarrow 2_1^+)$
^{150}Nd				
Exp.	0.130	0.381	1.539(14)	2.745(70)
Calc.	$0.146^{+0.022}_{-0.027}$	$0.461^{+0.057}_{-0.068}$	$1.579^{+0.131}_{-0.101}$	$2.918^{+0.309}_{-0.250}$
^{150}Sm				
Exp.	0.334	0.773	0.937(145)	1.351(31)
Calc.	$0.301^{+0.041}_{-0.062}$	$0.789^{+0.059}_{-0.094}$	$1.112^{+0.081}_{-0.054}$	$1.913^{+0.226}_{-0.134}$
^{136}Xe				
Exp.	1.313	1.694	0.011	0.230(9)
Calc.	$2.872^{+0.069}_{-0.072}$	$5.864^{+0.117}_{-0.129}$	$0.224^{+0.004}_{-0.004}$	$0.364^{+0.008}_{-0.009}$
^{136}Ba				
Exp.	0.819	1.551	0.119(51)	0.464(9)
Calc.	$1.756^{+0.065}_{-0.086}$	$3.548^{+0.195}_{-0.200}$	$0.278^{+0.019}_{-0.018}$	$0.451^{+0.020}_{-0.021}$

index i runs over all the physical quantities \mathbf{D} that are employed to refine the distribution of the parameters \mathbf{C} . In the calculation of the posterior of $M^{0\nu}$, we consider additionally

the constraints from excitation energies E_x and $E2$ transition strengths in (48), as well as the emulator errors of the SP-CDFT for the \mathbf{D} .

The conditional probability $p(\mathcal{O}|\mathbf{C})$ in (45) is given by

$$p(\mathcal{O}|\mathbf{C}) \propto \exp\left(-\frac{[\mathcal{O} - \mathcal{O}^{\text{em}}(\mathbf{C})]^2}{\sigma_{\text{em}}^2}\right), \quad (49)$$

where $\mathcal{O}^{\text{em}}(\mathbf{C})$ is the prediction of the emulator for the quantity \mathcal{O} using the parameter set \mathbf{C} , and σ_{em} is the emulator error of this quantity.

Figure 12 shows the posterior distribution $p(\mathbf{C}|\mathcal{D})$ of each parameter c_l , where the data \mathcal{D} contain the empirical values of the nuclear-matter properties Θ_{sat} at saturation density, those below saturation density Θ_{low} obtained from the many-body perturbation theory calculation based on a chiral NN and $3N$ potentials up to $N^3\text{LO}$ [85], and the data for the $B(E2 : 0_1^+ \rightarrow 2_1^+)$ of ^{136}Xe . Figure 13 shows the posterior distribution $p(\mathbf{C}|\mathcal{D})$ which is obtained similar to Fig. 12, but replacing the $B(E2 : 0_1^+ \rightarrow 2_1^+)$ of ^{136}Xe with that of ^{150}Nd . It is observed that the main peaks of the posterior distribution $p(\mathbf{C}|\mathcal{D})$ for most parameters derived from the $B(E2)$ data of ^{136}Xe are offset from their values in PC-PK1. In contrast, the parameters derived from the $B(E2)$ data of ^{150}Nd align well with the values in PC-PK1. This phenomenon can be understood from the observation that the $B(E2)$ of ^{150}Nd is much better reproduced by the MR-CDFT than that for ^{136}Xe , as detailed in Table III. It lists the median and uncertainties of the posteriors for the excitation energies of the 2_1^+ and 4_1^+ states and $E2$ transition strengths in the four nu-

clei. It is clear that the excitation energies of the deformed nuclei ^{150}Nd and ^{150}Sm are excellently reproduced, whereas those of the near-spherical nuclei ^{136}Xe and ^{136}Ba are overestimated. The ratio $R_{42} = E_x(4_1^+)/E_x(2_1^+) < 2$ in both ^{136}Xe and ^{136}Ba indicates that their $2_1^+, 4_1^+$ states are dominated by seniority coupling [98], which requires the inclusion of pair-breaking configurations into the MR-CDFT model space for accurate description. The non-collective excitation nature of the $2_1^+, 4_1^+$ states in ^{136}Xe and ^{136}Ba can also be inferred from the weak $E2$ transition strengths. With the posterior distribution, we finally derive the statistical uncertainties for the low-lying states, which are generally within 21% for excitation energies and 12% for $E2$ transition strengths.

Figure 14 illustrates the correlations derived from the posterior distributions of the parameters in Figs. 12 and 13. Compared to the correlation relations in Figs. 9 and 10, the correlations between the NME $M^{0\nu}$ and the excitation energies of $2_1^+, 4_1^+$ states, and $E2$ transition strengths in Fig. 14 are slightly weakened. For example, the Pearson coefficient between $M^{0\nu}$ and $E_x(2_1^+)$ in ^{150}Nd decreases from 0.93 to 0.84. The Pearson coefficient for the anti-correlation between $M^{0\nu}$ and $B(E2 : 0_1^+ \rightarrow 2_1^+)$ is changed from -0.93 to -0.85 . Despite these slight changes, the correlations remain robust, supporting the application of the Bayesian model averaging method for $0\nu\beta\beta$ studies[99]. As discussed in Ref. [64], the median value and uncertainties (determined by the 4th percentile and 96th percentile) for the NMEs are $5.51_{-0.26}^{+0.24}$ for ^{150}Nd , and $4.34_{-0.10}^{+0.09}$ for ^{136}Xe , in line with the values 5.60 and 4.32 by the PC-PK1 [90].

IV. SUMMARY

In this work, we have introduced the detailed formulation of subspace-projected covariant density functional theory (SP-CDFT), a novel approach that combines the eigenvector continuation (EC) method with the quantum-number projected generator coordinate method (GCM) within the framework of covariant density functional theory (CDFT). We have demonstrated the efficiency and accuracy of SP-CDFT as an emulator for multireference (MR)-CDFT in the study of nuclear low-lying states. The results show that the emulator errors for nuclear bulk properties are within a few tenths of a percent, while the errors for excitation energies and $E2$ transition strengths are generally about a few percent. Using SP-CDFT, we conducted a global sensitivity analysis of key physical quantities relative to the parameters of the energy density functional (EDF), including ground-state energy, proton radius, excitation energies of the 2_1^+ and 4_1^+ states, and $E2$ transition strengths for ^{136}Xe , ^{136}Ba , ^{150}Nd and ^{150}Sm . Our

findings reveal that the global sensitivity is predominantly influenced by the coupling constants α_S and α_V , which are associated with scalar and vector types of four-fermion contact interactions. Additionally, we examined in detail the variations in nuclear low-lying states and the nuclear matrix element (NME) $M^{0\nu}$ of $0\nu\beta\beta$ decay with respect to each EDF parameter, and found significant differences in the variation trends for the near spherical nuclei ^{136}Xe , ^{136}Ba and deformed nuclei ^{150}Nd and ^{150}Sm .

The development of SP-CDFT has enabled us to explore correlations among nuclear-matter properties, nuclear low-lying states, and the $M^{0\nu}$ of $0\nu\beta\beta$ decay and to quantify their statistical uncertainties using the Bayesian method. We found that the ground-state energies of finite nuclei are strongly correlated with the average nucleon energy E/A of nuclear matter. Moreover, the incompressibility K and the ground-state proton radius R_p are anti-correlated with E/A and the saturation density ρ_0 , respectively. These correlation patterns are consistent across ^{150}Nd and ^{136}Xe . Furthermore, we observed that the excitation energies of the 2_1^+ and 4_1^+ states are anti-correlated with $E2$ transition strengths, with strong correlations in the deformed nuclei ^{150}Nd and ^{150}Sm , but weaker correlations in the spherical nuclei ^{136}Xe and ^{136}Ba . In particular, our study has shown that the $B(E2 : 0_1^+ \rightarrow 2_1^+)$ could be either positive or negative correlated with the proton radius R_p of the ground state. Notably, we identified strong correlations between $M^{0\nu}$ and the excitation energies of the 2_1^+ and 4_1^+ states, as well as $E2$ transition strengths, providing a foundation for employing Bayesian model averaging methods in $0\nu\beta\beta$ studies. Additionally, we found that the statistical uncertainties from the nine parameters are within 21% for excitation energies and 12% for $E2$ transition strengths. Future work will focus on improving the SP-CDFT for near spherical nuclei and refining nuclear EDFs based on data for nuclear low-lying states.

ACKNOWLEDGMENTS

We thank K. Hagino, H. Hergert, W.G. Jiang, C.F. Jiao, X.L. Zhang, and Y.N. Zhang for their fruitful discussions, and C. Drischler for providing nuclear matter properties from ab initio calculations. This work is partly supported by the National Natural Science Foundation of China (Grant Nos. 12141501 and 12275369), the Guangdong Basic and Applied Basic Research Foundation (2023A1515010936), and the Fundamental Research Funds for the Central Universities, Sun Yat-sen University. We also acknowledge the Beijing Super Cloud Computing Center (BSCC) for providing HPC resources.

-
- [1] M. Bender, P.-H. Heenen, and P.-G. Reinhard, *Rev. Mod. Phys.* **75**, 121 (2003).
 [2] D. Vretenar, A. Afanasjev, G. Lalazissis, and P. Ring, *Physics Reports* **409**, 101 (2005).

- [3] J. Meng, H. Toki, S. G. Zhou, S. Q. Zhang, W. H. Long, and L. S. Geng, *Prog. Part. Nucl. Phys.* **57**, 470 (2006), arXiv:nucl-th/0508020.

- [4] J. E. Drut, R. J. Furnstahl, and L. Platter, *Prog. Part. Nucl. Phys.* **64**, 120 (2010), arXiv:0906.1463 [nucl-th].
- [5] W. Kohn and L. J. Sham, *Phys. Rev.* **140**, A1133 (1965).
- [6] G. A. Lalazissis, S. Raman, and P. Ring, *Atom. Data Nucl. Data Tabl.* **71**, 1 (1999).
- [7] L. Geng, H. Toki, and J. Meng, *Progress of Theoretical Physics* **113**, 785 (2005), <https://academic.oup.com/ptp/article-pdf/113/4/785/5123587/113-4-785.pdf>.
- [8] J. Erler, N. Birge, M. Kortelainen, W. Nazarewicz, E. Olsen, A. M. Perhac, and M. Stoitsov, *Nature* **486**, 509 (2012).
- [9] S. E. Agbemava, A. V. Afanasjev, and A. Taninah, *Phys. Rev. C* **99**, 014318 (2019), arXiv:1811.11473 [nucl-th].
- [10] P. Guo et al. (DRHBc Mass Table), *Atom. Data Nucl. Data Tabl.* **158**, 101661 (2024), arXiv:2402.02935 [nucl-th].
- [11] B.-A. Li, L.-W. Chen, and C. M. Ko, *Phys. Rept.* **464**, 113 (2008), arXiv:0804.3580 [nucl-th].
- [12] A. V. Afanasjev and S. E. Agbemava, *Phys. Rev. C* **93**, 054310 (2016), arXiv:1604.07296 [nucl-th].
- [13] J. Dobaczewski, W. Nazarewicz, and P. G. Reinhard, *J. Phys. G* **41**, 074001 (2014), arXiv:1402.4657 [nucl-th].
- [14] T. Skyrme, *Nucl. Phys.* **9**, 615 (1959).
- [15] D. Vautherin and D. M. Brink, *Phys. Rev. C* **5**, 626 (1972).
- [16] D. Gogny, P. Pires, and R. De Tourreil, *Phys. Lett. B* **32**, 591 (1970).
- [17] J. Decharge and D. Gogny, *Phys. Rev. C* **21**, 1568 (1980).
- [18] J. D. Walecka, *Annals Phys.* **83**, 491 (1974).
- [19] P. G. Reinhard, *Rept. Prog. Phys.* **52**, 439 (1989).
- [20] P. Ring, *Progress in Particle and Nuclear Physics* **37**, 193 (1996).
- [21] J. Meng, *Relativistic Density Functional for Nuclear Structure (WORLD SCIENTIFIC, 2016)* <https://www.worldscientific.com/doi/pdf/10.1142/9872>.
- [22] A. Schwenk and J. Polonyi (2004) arXiv:nucl-th/0403011.
- [23] D. Gambacurta, L. Li, G. Colo, U. Lombardo, N. Van Giai, and W. Zuo, *Phys. Rev. C* **84**, 024301 (2011).
- [24] M. Grasso, D. Lacroix, and U. van Kolck, *Phys. Scripta* **91**, 063005 (2016).
- [25] C. J. Yang, M. Grasso, and D. Lacroix, *Phys. Rev. C* **96**, 034318 (2017), arXiv:1706.00258 [nucl-th].
- [26] J. Bonnard, M. Grasso, and D. Lacroix, *Phys. Rev. C* **98**, 034319 (2018), [Erratum: *Phys. Rev. C* **103**, 039901 (2021)], arXiv:1806.01084 [nucl-th].
- [27] H. Liang, Y. Niu, and T. Hatsuda, *Phys. Lett. B* **779**, 436 (2018), arXiv:1710.00650 [cond-mat.str-el].
- [28] S. Burrello, J. Bonnard, and M. Grasso, *Phys. Rev. C* **103**, 064317 (2021), arXiv:2103.05996 [nucl-th].
- [29] F. Marino, C. Barbieri, A. Carbone, G. Colò, A. Lovato, F. Pedriva, X. Roca-Maza, and E. Vigezzi, *Phys. Rev. C* **104**, 024315 (2021), arXiv:2103.14480 [nucl-th].
- [30] R. Navarro Pérez, N. Schunck, A. Dyhdalo, R. J. Furnstahl, and S. K. Bogner, *Phys. Rev. C* **97**, 054304 (2018), arXiv:1801.08615 [nucl-th].
- [31] L. Zurek, S. K. Bogner, R. J. Furnstahl, R. Navarro Pérez, N. Schunck, and A. Schwenk, *Phys. Rev. C* **109**, 014319 (2024), arXiv:2307.13568 [nucl-th].
- [32] S. Shen, H. Liang, W. H. Long, J. Meng, and P. Ring, arXiv:1904.04977 [nucl-th] (2019).
- [33] M. Grasso, *Prog. Part. Nucl. Phys.* **106**, 256 (2019), arXiv:1811.01039 [nucl-th].
- [34] R. J. Furnstahl, *Eur. Phys. J. A* **56**, 85 (2020), arXiv:1906.00833 [nucl-th].
- [35] S. Goriely and R. Capote, *Phys. Rev. C* **89**, 054318 (2014).
- [36] J. D. McDonnell, N. Schunck, D. Higdon, J. Sarich, S. M. Wild, and W. Nazarewicz, *Phys. Rev. Lett.* **114**, 122501 (2015), arXiv:1501.03572 [nucl-th].
- [37] S. E. Agbemava, A. V. Afanasjev, D. Ray, and P. Ring, *Phys. Rev. C* **89**, 054320 (2014), arXiv:1404.4901 [nucl-th].
- [38] P. Giuliani, K. Godbey, E. Bonilla, F. Viens, and J. Piekarewicz, (2022), arXiv:2209.13039 [nucl-th].
- [39] M. Salinas and J. Piekarewicz, *Phys. Rev. C* **107**, 045802 (2023), arXiv:2301.09692 [nucl-th].
- [40] X. Sun, Z. Miao, B. Sun, and A. Li, *Astrophys. J.* **942**, 55 (2023), arXiv:2205.10631 [astro-ph.HE].
- [41] J. M. Yao, “Symmetry Restoration Methods,” in *Handbook of Nuclear Physics*, edited by I. Tanihata, H. Toki, and T. Kajino (2022) pp. 1–36, arXiv:2204.12126 [nucl-th].
- [42] P. Ring and P. Schuck, *The nuclear many-body problem* (Springer-Verlag, New York, 1980).
- [43] M. Bender and P.-H. Heenen, *Phys. Rev. C* **78**, 024309 (2008).
- [44] T. R. Rodríguez and J. L. Egido, *Phys. Rev. C* **81**, 064323 (2010).
- [45] J. M. Yao, J. Meng, P. Ring, and D. Vretenar, *Phys. Rev. C* **81**, 044311 (2010).
- [46] T. Nikšić, D. Vretenar, and P. Ring, *Prog. Part. Nucl. Phys.* **66**, 519 (2011).
- [47] L. M. Robledo, T. R. Rodríguez, and R. R. Rodríguez-Guzmán, *J. Phys. G* **46**, 013001 (2019), arXiv:1807.02518 [nucl-th].
- [48] J. A. Sheikh, J. Dobaczewski, P. Ring, L. M. Robledo, and C. Yannouleas, *Journal of Physics G: Nuclear and Particle Physics* **48**, 123001 (2021).
- [49] X.-X. Sun and S.-G. Zhou, *Phys. Rev. C* **104**, 064319 (2021), arXiv:2107.05925 [nucl-th].
- [50] E. F. Zhou and J. M. Yao, *Int. J. Mod. Phys. E* **32**, 2340011 (2023), arXiv:2309.09488 [nucl-th].
- [51] T. R. Rodríguez and G. Martínez-Pinedo, *Phys. Rev. Lett.* **105**, 252503 (2010).
- [52] L. S. Song, J. M. Yao, P. Ring, and J. Meng, *Phys. Rev. C* **90**, 054309 (2014).
- [53] J. M. Yao, J. Meng, Y. F. Niu, and P. Ring, *Prog. Part. Nucl. Phys.* **126**, 103965 (2022), arXiv:2111.15543 [nucl-th].
- [54] Y. K. Wang, P. W. Zhao, and J. Meng, *Phys. Lett. B* **855**, 138796 (2024), arXiv:2403.06455 [nucl-th].
- [55] T. Chupp, P. Fierlinger, M. Ramsey-Musolf, and J. Singh, *Rev. Mod. Phys.* **91**, 015001 (2019), arXiv:1710.02504 [physics.atom-ph].
- [56] G. Arrowsmith-Kron et al., *Rept. Prog. Phys.* **87**, 084301 (2024), arXiv:2302.02165 [nucl-ex].
- [57] N. Severijns, M. Beck, and O. Naviliat-Cuncic, *Rev. Mod. Phys.* **78**, 991 (2006), arXiv:nucl-ex/0605029.
- [58] R. Alarcon et al. (2022) arXiv:2203.08103 [hep-ph].
- [59] V. Cirigliano et al., (2022), arXiv:2203.12169 [hep-ph].
- [60] M. Horoi, A. Neacsu, and S. Stoica, *Phys. Rev. C* **106**, 054302 (2022), arXiv:2203.10577 [nucl-th].
- [61] M. Horoi, A. Neacsu, and S. Stoica, *Phys. Rev. C* **107**, 045501 (2023), arXiv:2302.03664 [nucl-th].
- [62] J. M. Yao, B. Bally, J. Engel, R. Wirth, T. R. Rodríguez, and H. Hergert, *Phys. Rev. Lett.* **124**, 232501 (2020).
- [63] A. Belley, T. Miyagi, S. R. Stroberg, and J. D. Holt (2022).
- [64] X. Zhang, C. C. Wang, C. R. Ding, and J. M. Yao, (2024), arXiv:2408.00691 [nucl-th].
- [65] D. Frame, R. He, I. Ipsen, D. Lee, D. Lee, and E. Rrapaj, *Phys. Rev. Lett.* **121**, 032501 (2018).
- [66] M. C. Franzke, A. Tichai, K. Hebeler, and A. Schwenk, *Phys. Lett. B* **830**, 137101 (2022), arXiv:2108.02824 [nucl-th].
- [67] T. Sowiński and M. A. Garcia-March, *Phys. Rev. C* **106**, 024002 (2022), arXiv:2202.07493 [cond-mat.quant-gas].
- [68] V. V. Baran and D. R. Nichita, *Phys. Rev. B* **107**, 144503 (2023), arXiv:2212.14313 [cond-mat.supr-con].

- [69] M. C. Franzke, A. Tichai, K. Hebeler, and A. Schwenk, *Phys. Rev. C* **109**, 024311 (2024), arXiv:2302.08373 [nucl-th].
- [70] Q. Y. Luo, X. Zhang, L. H. Chen, and J. M. Yao, *Phys. Rev. C* **110**, 014309 (2024).
- [71] A. Ekström and G. Hagen, *Phys. Rev. Lett.* **123**, 252501 (2019), arXiv:1910.02922 [nucl-th].
- [72] S. König, A. Ekström, K. Hebeler, D. Lee, and A. Schwenk, *Physics Letters B* **810**, 135814 (2020).
- [73] R. J. Furnstahl, A. J. Garcia, P. J. Millican, and X. Zhang, *Phys. Lett. B* **809**, 135719 (2020), arXiv:2007.03635 [nucl-th].
- [74] P. Demol, T. Duguet, A. Ekström, M. Frosini, K. Hebeler, S. König, D. Lee, A. Schwenk, V. Somà, and A. Tichai, *Phys. Rev. C* **101**, 041302 (2020), arXiv:1911.12578 [nucl-th].
- [75] C. Drischler, M. Quinonez, P. G. Giuliani, A. E. Lovell, and F. M. Nunes, *Phys. Lett. B* **823**, 136777 (2021), arXiv:2108.08269 [nucl-th].
- [76] D. Bai and Z. Ren, *Phys. Rev. C* **103**, 014612 (2021), arXiv:2101.06336 [nucl-th].
- [77] A. Sarkar and D. Lee, *Phys. Rev. Lett.* **126**, 032501 (2021).
- [78] C. Drischler, J. A. Melendez, R. J. Furnstahl, A. J. Garcia, and X. Zhang, *Front. in Phys.* **10**, 1092931 (2022), arXiv:2212.04912 [nucl-th].
- [79] T. Duguet, A. Ekström, R. J. Furnstahl, S. König, and D. Lee, (2023), arXiv:2310.19419 [nucl-th].
- [80] J. M. Yao, J. Meng, P. Ring, and D. P. Arteaga, *Phys. Rev. C* **79**, 044312 (2009).
- [81] E. F. Zhou, X. Y. Wu, and J. M. Yao, *Phys. Rev. C* **109**, 034305 (2024), arXiv:2311.15305 [nucl-th].
- [82] T. Burvenich, D. G. Madland, J. A. Maruhn, and P. G. Reinhard, *Phys. Rev. C* **65**, 044308 (2002), arXiv:nucl-th/0111012.
- [83] P. W. Zhao, Z. P. Li, J. M. Yao, and J. Meng, *Phys. Rev. C* **82**, 054319 (2010).
- [84] M. Dutra, O. Lourenço, S. S. Avancini, B. V. Carlson, A. Delfino, D. P. Menezes, C. Providência, S. Typel, and J. R. Stone, *Phys. Rev. C* **90**, 055203 (2014), arXiv:1405.3633 [nucl-th].
- [85] C. Drischler, R. J. Furnstahl, J. A. Melendez, and D. R. Phillips, *Phys. Rev. Lett.* **125**, 202702 (2020).
- [86] D. L. Hill and J. A. Wheeler, *Phys. Rev.* **89**, 1102 (1953).
- [87] R. Balian and E. Brezin, *Nuovo Cimento B Serie* **64**, 37 (1969).
- [88] T. Nikšić, D. Vretenar, and P. Ring, *Phys. Rev. C* **73**, 034308 (2006).
- [89] J. M. Yao, K. Hagino, Z. P. Li, J. Meng, and P. Ring, *Phys. Rev. C* **89**, 054306 (2014), arXiv:1403.4812 [nucl-th].
- [90] J. M. Yao, L. S. Song, K. Hagino, P. Ring, and J. Meng, *Phys. Rev. C* **91**, 024316 (2015).
- [91] S. Dutta and A. H. Gandomi, in *Handbook of Probabilistic Models*, edited by P. Samui, D. Tien Bui, S. Chakraborty, and R. C. Deo (Butterworth-Heinemann, 2020) pp. 369–381.
- [92] W. G. Jiang, A. Ekström, C. Forssén, G. Hagen, G. R. Jansen, and T. Papenbrock, *Phys. Rev. C* **102**, 054301 (2020), arXiv:2006.16774.
- [93] Z. H. Sun, A. Ekström, C. Forssén, G. Hagen, G. R. Jansen, and T. Papenbrock (2024) arXiv:2404.00058 [nucl-th].
- [94] M. Qiu, B.-J. Cai, L.-W. Chen, C.-X. Yuan, and Z. Zhang, *Phys. Lett. B* **849**, 138435 (2024), arXiv:2312.07031 [nucl-th].
- [95] I. Sobol, *Mathematics and Computers in Simulation* **55**, 271 (2001), the Second IMACS Seminar on Monte Carlo Methods.
- [96] I. Vernon, M. Goldstein, and R. Bower, *Bayesian Analysis* **5** (2010), 10.1214/10-BA524.
- [97] National Nuclear Data Center, “NuDat 2 Database,” (2020), <https://www.nndc.bnl.gov/nudat2>.
- [98] C. Qi, *Phys. Lett. B* **773**, 616 (2017), arXiv:1810.07747 [nucl-th].
- [99] V. Cirigliano *et al.*, (2022), arXiv:2203.12169 [hep-ph].